University of Alberta

Variability in Summer Anticyclonic Activity over the Canadian Arctic Archipelago and west Greenland in the late 20th/early 21st centuries, and its impact on the firn stratigraphy of the Devon Ice Cap

by

Peter Bezeau

A thesis submitted to the Faculty of Graduate Studies and Research
in partial fulfillment of the requirements for the degree of

Master of Science

Earth and Atmospheric Sciences

©Peter Bezeau
Fall 2013
Edmonton, Alberta

Abstract

Significant summer warming over the Canadian Arctic Archipelago (CAA) is linked to a doubling in the frequency of anticyclonic circulation over the region since 2007. The frequency of positive anomalies in summer 500 hPa geopotential height is related to Arctic sea ice volume/thickness in April, May and June (1979-2012) and to poleward eddy heat flux in June. More frequent summer anticyclonic circulation over the CAA has caused more intense and sustained melt of ice caps and glaciers, and increased rates of mass loss. Based on 54 shallow cores recovered from elevations of 1400-1900 m a.s.l. on the Devon Ice Cap between 2004 and 2012, firn layer thinning due to more rapid densification in a warmer climate can explain much of the reduction in ice cap surface height measured by repeat airborne laser altimetry between 2004 and 2012 (-0.077 to -0.252 m a^{-1}).

Acknowledgements

Table of Contents

List of Table

List of Figures

List of Abbreviations

a.s.l.	Above sea level
a^{-1}	Per annum
AMO	Atlantic Multidecal Oscillation
AR5	IPCC Fifth Assessment Report
AWS	Automatic weather stations
CAA	Canadian Arctic Archipelago
BCC	Beijing Climate Center Climate Systems Model version 1.1
CanESM2	Canadian Centre for Climate Modelling and Analysis Earth Systems Model 2
CCSM4	National Center for Atmospheric Research Community Climate System Model 4
CGCMs	Coupled General circulation models
CMIP3	Coupled Model Intercomparison Project Phase 3
CMIP5	Coupled Model Intercomparison Project Phase 5
DMI	Danish Meteorological Institute
EOF	Empirical orthogonal function
ERSST V3b	Extended Reconstructed Sea Surface Temperatures Version 3b
ESGF	Earth System Grid Federation
GPH	Geopotential height
GPR	Ground penetrating radar
hPa	Hectopascal
IR	Infrared (light with wavelengths between 330 nm and 1200 nm)
kOhm	1000 ohms
MAAT	Mean annual air temperature
MPI-ESM-LR	Max Planck Institute for Meteorology Earth Systems Model - Low Resolution
NCEP	National Centers for Environmental Prediction and the National Center for Atmospheric Research Reanalysis 1 project
NOAA	National Oceanic and Atmospheric Administration
NOI	Nodes of interest
NorESM	Norwegian Climate Centre Earth Systems Model 1-M
NSIDC	National Snow and Ice Data Center
PC	Principal components
PIOMAS	Pan-Arctic Ice Ocean Modeling and Assimilation System
RCP	Representative Concentration Pathways
RMSE	Root mean square error
SCE	Snow cover extent
SMB	Surface mass balance (glacier)
SOM	Self-organizing map
SST	Sea surface temperature
VIF	Variance inflation factor
w.e.	Water equivalent

Chapter 1

1.1 Motivation

Annual changes in the mass balance of Canadian Arctic glaciers are strongly influenced by variations in summer climate (Oerlemans & Reichert, 2000; Braithwaite, 2005; Koerner, 2005). The climate in the Canadian Arctic is characterized by low inter-annual variability of winter precipitation and high inter-annual variability of summer air temperatures and melt conditions. Based on National Centers for Environmental Prediction and the National Center for Atmospheric Research Reanalysis 1 project data (NCEP) (Kalnay et al., 1996) (1948-2012), the last decade's summer mean air temperature over the Canadian Arctic Archipelago (CAA) at 700 hPa has been the highest in the modern record, with 2005 to 2012 being especially warm (Sharp et al., 2011; Bezeau et al., 2013). Additionally, melt records derived from the ice content of firn cores from four ice caps/glaciers in the CAA show that current melt rates are the highest in the last 4000 years, and comparable to those seen in the Holocene thermal maximum around 9000 years ago (Fisher et al., 2012; Zdanowicz et al., 2012). As a result of the extreme melting since 2005, Canadian Arctic ice caps and glaciers have emerged as the most important regional non-ice sheet source of global sea level rise (Gardner et al., 2011, 2013; Lenaerts et al. 2013).

In the Arctic as a whole, amplification processes create disproportionate warming or cooling (approximately 2 times greater than the mean global air temperature change) as a result of natural feedbacks that alter the net energy balance (Serreze & Barry, 2011). Therefore, small changes in the mean global air temperature resulting from natural variability and/or anthropogenic forcings can, in the case of warming, lead to more sustained and intense ablation of the Arctic cryosphere.

Summer air temperatures and atmospheric circulation patterns in the Arctic show a high degree of year-to-year variability (Richter-Menge, 2011; Overland et al. 2012). Despite this, very little research has focused on the mechanisms underlying the regional variability. Understanding of the temporal and spatial patterns associated with past regional variability has historically been used to provide a context for what to expect in the future, as well as to provide a baseline against which to evaluate the possibility of regime shifts due to anthropogenic forcing of the climate system. In order to project the future evolution of Canadian Arctic glaciers and its implications for global mean sea level, it has become important to compare historic trends in the variability of atmospheric circulation found in climate reanalyses with the trends found in the output from climate models forced by historical and projected future greenhouse gas concentrations.

1.2 Summer anticyclonic circulation variability in the 20th and 21st century

In the 50 year CAA glacier mass balance record, the most negative measured balances prior to 2005 were recorded in the early 1960s and were linked to more persistent positive 500 hPa geopotential height (GPH) anomalies over the region during the summer melt season (Alt, 1978; 1979; 1987). Since 2007, very strong positive 500 hPa GPH anomalies have been observed over Greenland and the Eastern CAA in the summer months and these coincide with the most recent and largest observed glacier mass losses in the observational record (Sharp et al, 2011; Overland et al, 2012, Gascon et al., 2013; Fettweis et al., 2013; Hanna et al., 2013; Tedesco et al., 2013). For both periods, the negative mass balances have been associated with positive GPH anomalies that are analogous with anomalous anticyclonic circulation, which promotes the regional advection of warm air into the western Arctic and maximizes the shortwave radiation incident on the surface.

To evaluate the frequency and persistence of summer positive 500 hPa GPH anomalies through the observational record, we used NCEP climate reanalysis (1948-2012). To assess the ability of global climate models to simulate historic trends in summer positive 500 hPa GPH anomalies and project those trends into the future, climate model outputs from a selection of the Coupled Model Intercomparison Project Phase 5 (CMIP5) (1950-2025) models (Taylor et al., 2012) are compared with NCEP data using a self-organizing map (SOM) (Kohonen, 2001). Capable of capturing the probability of rare events and non-linear trends, the SOM provides a significant advantage for climate research over traditional classification methods such as principal components (PC) and empirical orthogonal function (EOF) analyses (Reusch et al., 2005; Reusch, 2010). Using daily summer 500 hPa GPH anomalies as SOM input data, generalized circulation patterns are calculated along with their frequency of occurrence. The SOM creates the ability to directly compare the spatial and temporal predictions of the CMIP5 models with the NCEP reanalysis under both historical and future emissions scenarios. Additionally, using the probability of occurrence of each generalized circulation pattern, further analyses can be undertaken to identify potential drivers of climatic change. Here, we explore the contributions of sea ice extent, sea ice volume, northern hemisphere snow cover extent and meridional heat advection to historical changes in NCEP summer 500 hPa GPH anomalies over the CAA and western Greenland.

1.3 Firn profile response to recent climate warming on Devon Ice Cap

On Arctic ice caps and glaciers, an observable impact of warmer air temperatures and albedo feedbacks has been an increase in the intensity and duration of summer melt (Box et al., 2012; Gascon et al., 2013; Wang et al., 2013). In the accumulation zone, the area where total annual accumulation exceeds total annual ablation, the imprint of rising air temperatures should be visible in the physical and thermal characteristics of the firn profile. The firn layer is the seasonal snow accumulated on a glacier over a period of years that survives melting and is in the process of being transformed to glacier ice. It

3

has density and physical characteristics between those of fresh snow and glacier ice. Prior to the 21st century, densification of the firn column occurred at relatively steady rates due to compaction under conditions of relatively consistent temperature and accumulation (Hörhold et al., 2011). However, since the mid-2000s, the fraction of ice in the firn layer, formed by the refreezing of percolating meltwater, is believed to have increased significantly due to warmer air temperatures and higher melt rates. This has implications for the rate of firn densification, firn temperatures, the interpretation of firn stratigraphy in ground penetrating radar (GPR) surveys, and glacier mass balance estimates made using repeat airborne or satellite altimetry (Parry et al., 2007; Humphrey, Harper & Pfeffer, 2012).

1.4 Thesis outline

Chapter 2 applies the SOM approach to the analysis of daily summer 500 hPa GPH anomaly fields derived from NCEP reanalysis (1948-2012) and five CMIP5 models (1950-2025). The results of the SOM analysis are first used to establish the relationship between NCEP 500 hPa GPH anomalies, four glacier mass balance records from the CAA (1960s-2011) and surface air temperature measurements made at five weather stations in the CAA and three weather stations on the west coast of Greenland (1948-2012). Due to the importance of summer atmospheric circulation for glacier mass balance in the CAA, the capability of the CMIP5 models to reproduce the patterns and frequencies of 500 hPa GPH anomalies found in NCEP reanalysis is evaluated. Finally, the NCEP SOM results are used to evaluate the influence of sea ice extent, sea ice volume, northern hemisphere snow cover extent and meridional heat advection on the rate and pattern of recent climate warming and the development of positive 500 hPa GPH anomalies over the CAA and western Greenland.

Chapter 3 presents the results of a shallow firn coring campaign conducted in the spring of 2012. Cores ranging in depth from 5-15 m were recovered from 20 sites that had

been cored previously between 2004 and 2011. To evaluate the impact on the firn profile of the anomalously high summer melt rates observed since 2005, profiles of physical properties and temperature from 2004-2006 and 2012 are compared. The accuracies of empirically modeled firn density profiles, based on the assumption of steady state climatic conditions, are evaluated at 3 sites to determine if they continue to be capable of producing firn density profiles that replicate in situ measurements. Finally, surface height changes measured by airborne laser altimetry are compared with surface height changes calculated from firn density changes to evaluate the contribution of more rapid firn densification to the altimetrically measured surface height changes between 2004 and 2012.

A version of chapter 3 has been published. Bezeau et al. 2013. Firn profile changes in response to extreme 21st century melting at Devon Ice Cap, Nunavut, Canada. *Journal of Glaciology*, 59(217).

1.5 References

Alt, B. T. (1978). Synoptic climate controls of mass-balance variations on Devon Island Ice Cap. *Arctic and Alpine Research,* 61-80.

Alt, B. T. (1979). Investigation of summer synoptic climate controls on the mass balance of Meighen Ice Cap. *Atmosphere-Ocean, 17*(3), 181-199.

Alt, B. T. (1987). Developing synoptic analogs for extreme mass balance conditions on Queen Elizabeth Island Ice Caps. *Journal of Applied Meteorology, 26*, 1605-1623.

Bezeau, P., Sharp, M., Burgess, D., & Gascon, G. (2013). Firn profile changes in response to extreme 21st century melting at Devon Ice Cap, Nunavut, Canada. *Journal of Glaciology, 59*(217), 981-991.

Box, J., Fettweis, X., Stroeve, J., Tedesco, M., Hall, D., & Steffen, K. (2012). Greenland Ice Sheet albedo feedback: Thermodynamics and atmospheric drivers. *The Cryosphere, 6*(4), 821-839.

Braithwaite, R. J. (2005). Mass-balance characteristics of Arctic glaciers. *Annals of Glaciology, 42*(1), 225-229.

Fettweis, X., Hanna, E., Lang, C., Belleflamme, A., Erpicum, M., & Gallée, H. (2013).

Important role of the mid-tropospheric atmospheric circulation in the recent surface melt increase over the Greenland Ice Sheet. *The Cryosphere , 7.*

Fisher, D., Zheng, J., Burgess, D., Zdanowicz, C., Kinnard, C., Sharp, M., et al. (2012). Recent melt rates of Canadian Arctic ice caps are the highest in four millennia. *Global and Planetary Change, 84*, 3-7.

Gardner, A. S., Moholdt, G., Cogley, J. G., Wouters, B., Arendt, A. A., Wahr, J., et al. (2013). A reconciled estimate of glacier contributions to sea level rise: 2003 to 2009. *Science, 340*(6134), 852-857.

Gardner, A. S., Moholdt, G., Wouters, B., Wolken, G. J., Burgess, D. O., Sharp, M. J., et al. (2011). Sharply increased mass loss from glaciers and ice caps in the Canadian Arctic Archipelago. *Nature, 473*(7347), 357-360.

Gascon, G., Sharp, M., & Bush, A. (2013). Changes in melt season characteristics on Devon Ice Cap, Canada, and their association with the arctic atmospheric circulation. *Annals of Glaciology, 54*, 101-110.

Hanna, E., Fettweis, X., Mernild, S. H., Cappelen, J., Ribergaard, M. H., Shuman, C. A., et al. (2013). Atmospheric and oceanic climate forcing of the exceptional Greenland Ice Sheet surface melt in summer 2012. *International Journal of Climatology.*

Hörhold, M., Kipfstuhl, S., Wilhelms, F., Freitag, J., & Frenzel, A. (2011). The densification of layered polar firn. *Journal of Geophysical Research: Earth Surface (2003–2012), 116*(F1).

Humphrey, N. F., Harper, J. T., & Pfeffer, W. T. (2012). Thermal tracking of meltwater retention in Greenland's accumulation area. *Journal of Geophysical Research: Earth Surface (2003–2012), 117*(F1).

Kalnay, E., Kanamitsu, M., Kistler, R., Collins, W., Deaven, D., Gandin, L., et al. (1996). The NCEP/NCAR 40-year reanalysis project. *Bulletin of the American Meteorological Society, 77*(3), 437-471.

Koerner, R. M. (2005). Mass balance of glaciers in the Queen Elizabeth Islands, Nunavut, Canada. *Annals of Glaciology, 42*(1), 417-423.

Kohonen, T. (2001). Self-organizing maps, vol. 30 of springer series in information sciences.

Lenaerts, J., Angelen, J. H., Broeke, M. R., Gardner, A. S., Wouters, B., & Meijgaard, E. (2013). Irreversible mass loss of Canadian Arctic Archipelago glaciers. *Geophysical Research Letters*,40, 1-5*.*

Oerlemans, J., & Reichert, B. (2000). Relating glacier mass balance to meteorological data by using a seasonal sensitivity characteristic. *Journal of Glaciology, 46*(152), 1-6.

Overland, J. E., Francis, J. A., Hanna, E., & Wang, M. (2012). The recent shift in early summer Arctic atmospheric circulation. *Geophysical Research Letters, 39*(19).

Parry, V., Nienow, P., Mair, D., Scott, J., Hubbard, B., Steffen, K., et al. (2007). Investigations of meltwater refreezing and density variations in the snowpack and firn within the percolation zone of the Greenland Ice Sheet. *Annals of Glaciology, 46*(1), 61-68.

Reusch, D. B. (2010). Nonlinear climatology and paleoclimatology: Capturing patterns of variability and change with self-organizing maps. *Physics and Chemistry of the Earth, Parts A/B/C, 35*(9), 329-340.

Reusch, D. B., Alley, R. B., & Hewitson, B. C. (2005). Relative performance of self-organizing maps and principal component analysis in pattern extraction from synthetic climatological data. *Polar Geography, 29*(3), 188-212.

Richter-Menge, J. (2011). *Arctic report card 2010* DIANE Publishing, Retrieved from http://www.arctic.noaa.gov/reportcard/.

Serreze, M. C., & Barry, R. G. (2011). Processes and impacts of arctic amplification: A research synthesis. *Global and Planetary Change, 77*(1), 85-96.

Sharp, M., Burgess, D. O., Cogley, J. G., Ecclestone, M., Labine, C., & Wolken, G. J. (2011). Extreme melt on Canada's Arctic ice caps in the 21st century. *Geophysical Research Letters, 38*(11) .

Taylor, K. E., Stouffer, R. J., & Meehl, G. A. (2012). An overview of CMIP5 and the experiment design. *Bulletin of the American Meteorological Society, 93*(4), 485-498.

Tedesco, M., Fettweis, X., Mote, T., Wahr, J., Alexander, P., Box, J., et al. (2013). Evidence and analysis of 2012 Greenland records from spaceborne observations, a regional climate model and reanalysis data. *The Cryosphere Discussions, 6.*

Wang, L., Derksen, C., Brown, R., & Markus, T. (2013). Recent changes in pan‐Arctic melt onset from satellite passive microwave measurements. *Geophysical Research Letters,* 40, 522-528.

Zdanowicz, C., Smetny‐Sowa, A., Fisher, D., Schaffer, N., Copland, L., Eley, J., et al. (2012). Summer melt rates on Penny Ice Cap, Baffin Island: Past and recent trends and implications for regional climate. *Journal of Geophysical Research: Earth Surface (2003–2012), 117*(F2).

Chapter 2

2.1 Introduction

Measurements of the mass balance of glaciers and ice caps in the Canadian Arctic Archipelago (CAA) have shown a strong negative trend since 2005 (Gardner et al., 2011; Sharp et al., 2011; Lenaerts et al. 2013). As a result, the Canadian Arctic has become the most important non-ice sheet source of eustatic sea level rise (Gardner et al., 2013). The most negative mass balance years in this period have been associated with the development of ridges of high pressure over Greenland and the Eastern CAA in the summer months, which promote the poleward advection of warm air into the western Arctic and maximize the incoming shortwave radiation incident at the air-ice interface (Alt, 1978; Sharp et al, 2011; Overland et al, 2012, Gascon et al., 2013; Fettweis et al., 2013; Tedesco et al., 2013). Considering the CAA climate is characterized by low interannual variability of winter accumulation and high interannual variability of summer temperatures (Oerlemans & Reichert, 2000; Braithwaite, 2005; Koerner, 2005), the future evolution of atmospheric circulation in the region during the summer months is critical to understanding glacier mass balance and the future contribution of the CAA to eustatic sea level rise (Gardner & Sharp 2007; Gascon et al., 2013).

Prior to the 2005-2012 period of anomalously high melt, the most recent period of anomalously high melt conditions in the CAA was the late 1950s and early 1960s (Fisher et al., 2012; Zdanowicz et al., 2012). Work on the Devon Ice Cap by Alt (1978), that was later expanded to the CAA (Alt, 1987), found the intrusions of high pressure ridges over the CAA in summers of the early 1960s that produced intense melt conditions and strongly negative mass balances. More recently, Gascon et al. (2013) compared the periods 2000-2004 with 2005-2010, and showed that positive 500 hPa geopotential height (GPH) anomalies in 2005-2010 increased melt energy at the surface of the lower accumulation zone (1400 m a.s.l.) of the Devon Ice Cap, raising annual

meltwater production on average from 74 cm w.e. to 133 cm w.e. between the two periods. Therefore, it is important to evaluate the historic trend and future predictions of the prevalence of positive 500 hPa GPH anomalies over the CAA, as they are strongly linked to glacier mass balance variability in the CAA.

To date, no study of 500 hPa GPH anomalies has been conducted focusing on the CAA over both the entire observational period (1948-2012) and future scenarios. The only comparable research has been done for Greenland, where 500 hPa GPH from NCEP and ERA-40 climate reanalyses were compared with modeled 500 hPa GPH from the World Climate Research Programme's (WCRP) Coupled Model Intercomparison Project Phases 3 (CMIP3) and 5 (CMIP5) (Belleflamme et al., 2012). During the summer months, no significant change was found in the frequency of pattern occurrence between the four time periods 1961-1990, 2011-2040, 2041-2070 and 2071-2100. However, a previously unobserved generalized atmospheric circulation pattern (the Arctic Dipole) has occurred in the early summer from 2007 to 2012 (Overland et al., 2012). The Arctic Dipole is characterized by relatively high sea-level pressures over the Beaufort Sea (extending into the CAA) and coincident low sea-level pressures over the Siberian Arctic. Overland et al. (2012) suggested enhanced Arctic warming due to decreased sea ice extent and decreased Northern Hemisphere spring snow cover extent (SCE) as a possible driver that could be, at least in part, responsible for the change in atmospheric circulation after 2007. Record breaking decreases in end of summer Arctic sea ice extent and since 2007 are important to consider as possible causes of the anomalous atmospheric circulation patterns, as they are important drivers of atmospheric circulation variability in the Arctic and Northern midlatitudes (Serreze & Barry, 2011; Francis & Vavrus, 2012; Screen et al. 2012). While increased meridional heat advection, decreased Northern Hemisphere snow cover extent, and decreased sea ice extent and volume are all plausible drivers for the changes in atmospheric circulation since 2007, direct evidence of a physical process that would increase air temperatures,

resulting in positive summer GPH anomalies over the CAA and Greenland, has remained elusive. Here, we look to answer to two questions.

1) Does the relationship between the frequency of positive summer 500 hPa GPH anomalies and negative CAA glacier surface mass balance (SMB) exist over the full observational record (1948-2012)?

2) Can the frequency of positive summer 500 hPa GPH anomalies over the CAA be predicted from measurements of sea ice extent, sea ice volume, Northern Hemisphere SCE and meridional heat advection?

In this paper, the Self-Organizing Map (SOM), a higher-order unsupervised classification tool capable of detecting non-linear change in climatological data sets, is applied to daily summer 500 hPa GPH anomalies calculated from the National Centers for Environmental Prediction and the National Center for Atmospheric Research Reanalysis 1 (NCEP) project (1948-2012) (Kalnay et al., 1996) and five CMIP5 Coupled General Circulation Models (CGCM) spanning 1950-2025 (Taylor et al. 2012). The output from the SOM allows comparisons of the patterns, frequency and persistence of 500 hPa GPH anomalies with spring and summer monthly mean surface air temperature measurements made at eight long running weather stations in the Canadian Arctic and on the west coast of Greenland and four 50 year observational annual SMB records from ice masses in the CAA. Additionally, the SOM output is used to investigate the relationships between the variability of summer 500 hPa GPH anomalies over western Greenland and the CAA, monthly estimates of meridional heat advection into the CAA and Baffin Bay, monthly North Atlantic sea surface temperature (SST) anomalies, monthly sea ice extent and volume, and monthly Northern Hemisphere SCE. The results and discussion sections of the paper present two complementary narratives. The first describes patterns of positive 500 hPa GPH anomalies over the CAA and western Greenland found in the NCEP data set and explores their impact on both surface air temperatures in the CAA and western

Greenland, and glacier SMB in the CAA. It also evaluates the capability of the CMIP5 models to reproduce the patterns and frequencies of 500 hPa GPH anomalies found in the NCEP data. The second narrative evaluates the relative importance of the various hypothesized drivers of Arctic circulation change (meridional heat advection, Northern Hemisphere SCE, sea ice extent and sea ice volume) with the goal of suggesting an underlying physical mechanism for the observed changes in summer Arctic atmospheric circulation since 2007.

2.2 Data sets

2.2.1 Geopotential heights

To characterize variability in atmospheric circulation patterns, Northern Hemisphere daily summer (June, July and August) 500 hPa GPH anomaly fields were calculated for 1948-2012 from the NCEP R1 Reanalysis on its native 2.5° x 2.5° grid using the 1951-2010 climatology as a reference (Kalnay et al., 1996). A 60 year climatology was chosen to avoid classification biases caused by a climatology that preferentially sampled either a warmer or cooler period in the Arctic. To test the hypothesis that atmospheric thermal expansion, resulting in a systematic increase in GPH that could bias the SOM classification, does not impose a dominant trend on the 500 hPa GPH anomalies, the slope of the linear regression of the GPH anomalies with respect to time, and the standard deviation of GPH anomalies are calculated for each grid cell and averaged across the northern hemisphere. Based on the regression, the increase in 500 hPa GPH anomalies from 1948-2012 was 17 m, while the standard deviation of the anomalies was 61 m. As the daily variability in 500 hPa GPH anomalies was much greater than the long term thermally induced rise in GPH anomalies, the SOM algorithm should produce robust classifications of 500 hPa GPH anomalies throughout the time domain.

Given the potential for erroneous results in climate reanalysis (Sterl, 2004; Bromwich & Wang, 2005; Screen & Simmonds, 2011), particularly in the high Arctic where observations are limited, radiosonde data from the Integrated Global Radiosonde Archive (Durre et al., 2006) were used to validate the frequency of 500 hPa positive GPH anomalies at two stations in the CAA (Resolute (1948-2012) and Alert (1951-2012)) and one on the west coast of Greenland (Aasiaat (1964-2012)) (see Figure 2-1). Twice-daily observations were averaged to produce daily geopotential heights, and anomalies were calculated relative to the 1964-2010 climatology (dictated by the length of record available for Aasiaat). The annual frequency of summer high pressure events was calculated by identifying the number of days per summer with 500 hPa geopotential heights greater than one standard deviation above the mean. This method was chosen to allow for comparison of the frequency of observed GPH anomalies and the frequency of GPH anomalies derived from NCEP using the SOM algorithm.

To produce reasonable estimates for the contribution of CAA glaciers and ice caps to global sea level change, a CGCM must be able to accurately represent the patterns and frequency of summer atmospheric circulation found in climate reanalysis (Marzeion et al., 2012; Fettweis, 2013; Lenaerts et al., 2013). To test their capabilities in this regard, data from five CMIP5 CGCMs, prepared for the Intergovernmental Panel on Climate Change (IPCC) Fifth Assessment Report (AR5), were analyzed using the SOM algorithm. The models used are the Beijing Climate Center Climate Systems Model version 1.1 (BCC), Canadian Centre for Climate Modelling and Analysis Earth Systems Model 2 (CanESM2), National Center for Atmospheric Research Community Climate System Model 4 (CCSM4), Max Planck Institute for Meteorology Earth Systems Model - Low Resolution (MPI-ESM-LR) and Norwegian Climate Centre Earth Systems Model 1-M (NorESM) (Taylor et al., 2012). Based on the memory required to compute the SOMs, it is only feasible to compare five models with NCEP. The five models were chosen based on their ability to accurately reproduce historic atmospheric circulation patterns

12

over Greenland (Belleflamme et al., 2012). Daily 500 hPa GPH fields were downloaded from the Earth System Grid Federation (ESGF) data portal (http://pcmdi9.llnl.gov). The temporal coverage of daily GPHs used for all five models is 1950-2005 under historic forcings and 2006-2025 under the high greenhouse gas concentration trajectory 'Representative Concentration Pathway 8.5' (RCP85). The RCP85 prescribes global anthropogenic radiative forcings rising from ~2.2 W m^{-2} in 2005 to 8.5 W m^{-2} in 2100 (Meinshausen et al., 2011).

The period 1950-2025 was selected as the time domain for the CMIP5 simulations as a compromise between extending the study period to the point in time where CMIP5 models produce the sea ice extent minima and spring snow cover extents observed in 2012 (Stroeve et al., 2012; Wang & Overland, 2012; Derksen & Brown, 2012), while minimizing the effects of atmospheric thermal expansion due to climate warming. To input GPH fields from the CMIP5 models into the SOM, the fields were linearly regridded to match the 2.5° x 2.5° NCEP grid.

2.2.2 Surface air temperatures

Monthly mean daily surface air temperatures spanning 1948-2012 are available for five sites in the Canadian Arctic (Alert, Eureka, Coral Harbour, Cambridge Bay and Resolute) and three sites on the west coast of Greenland (Nuuk, Ilulissat and Upernavik) (see Figure 2-1). Data for the Canadian Arctic are available from Environment Canada's National Climate Data and Information Archive (http://climate.weatheroffice.gc.ca). For Greenland, surface air temperatures for 1948-2010 (Cappelen, 2011) were updated to 2012 with measurements from the Danish Meteorological Institute (DMI) Weather Archive (http://www.dmi.dk/dmi/index/gronland/vejrarkiv-gl.htm). Surface air temperature anomalies were calculated relative to the 1951-2010 climatology.

2.2.3 Surface mass balance

There are four long running glacier SMB records from the CAA (the Devon Ice Cap (Burgess & Koerner, 2012), Meighen Ice Cap (Burgess, 2012a), Melville Ice Cap (Burgess, 2012b), and the White Glacier (Cogley & Ecclestone, 2009)) (see Figure 2-1). These records begin in 1961, 1960, 1963 and 1960 respectively and end in the 2011 mass balance year (measured in the spring of 2012). The climate that governs the mass balance of the ice mass in the CAA is characterized by low interannual variability of winter accumulation and high interannual variability of summer melt (Oerlemans & Reichert, 2000; Braithwaite, 2005; Koerner, 2005). Therefore, the SMB records provide a proxy data source for summer atmospheric circulation patterns, as large negative SMB is associated with extreme melt conditions produced by more frequent anticyclonic circulation over the CAA (Alt, 1987; Gascon et al., 2013).

2.2.4 Meridional heat transport

Positive 700 hPa meridional wind anomalies promoted poleward heat advection into Baffin Bay between 2007 and 2012 (Overland et al. 2012). To evaluate the role of this anomalous meridional heat transport in the development of positive 500 hPa GPH anomalies, the eddy heat flux component of the total meridional heat flux equation was calculated.

$$\overline{vT} = \overline{v}\,\overline{T} + \overline{v'T'}$$

Here, the total meridional heat flux $(\overline{vT})$ is the sum of the stationary heat flux $(\overline{v}\,\overline{T})$ and the eddy heat flux $(\overline{v'T'})$ (Peixoto and Oort, 1992). The stationary heat flux represents the time averaged (climatological) poleward advection of heat, while the eddy heat flux represents the short term (synoptic scale) perturbations of poleward heat advection. The eddy heat flux, calculated using the monthly NCEP 500 hPa air temperatures and meridional wind component from 1948-2012 (Kalnay et al., 1996), represents the product of the meridional wind component anomaly and the air temperature anomaly with respect to the 1951-2010 climatology. A time series of the eddy heat flux is

calculated by taking the area weighted average for the domain 65°N-85°N and 250°E-330°E (see Figure 2-1), encompassing the CAA, Baffin Bay, western Greenland and the CAA.

2.2.5 Atlantic Multidecal Oscillation (AMO) index

Surface air temperature measurements in the Arctic correlate positively with the AMO index through the 20th century and early 21st century (Chylek et al., 2009; Hanna et al., 2012). As the AMO has been generally positive since the mid-1990s, and strongly positive since 2005, it could be related to the increase in 500 hPa GPH anomalies observed since 2007.

The AMO index characterizes North Atlantic SST variability (Enfield et al., 2001), and is defined as the monthly detrended, area weighted average sea surface temperature anomaly relative to the 1951-1980 climatology over the North Atlantic basin from 0°N to 75°N. The monthly AMO index from 1948-2012 is available from the National Oceanic and Atmospheric Administration's (NOAA) Earth Systems Research Laboratory (http://www.esrl.noaa.gov/). To maintain a consistent climatology throughout the analysis, the observed AMO was calculated for 1948-2012 from the Extended Reconstructed Sea Surface Temperatures Version 3b dataset (ERSST V3b) (Smith et al., 2008) using a 1951-2010 climatology. The two AMO indices have a correlation coefficient of 0.94 (p<0.01).

2.2.6 Sea ice extent and volume

The Arctic Sea Ice Index (http://nsidc.org/data/seaice_index/, 2013-04-25) from the National Snow and Ice Data Center (NSIDC) provides a measure of monthly pan-Arctic sea ice extent from 1979-2012 (Fetterer et al., 2002). To produce the Arctic Sea Ice Index, gridded sea ice concentrations are derived from DMSP SSM/I Daily Polar Gridded Sea Ice Concentrations and the Sea Ice Concentrations from Nimbus-7 SSMR

and DMSP SSM/I passive microwave data using the NASA Team algorithm (Cavalieri et al., 1984). Sea ice extent is then calculated from pixels containing ≥15% sea ice concentration.

Monthly Arctic sea ice volume for 1979 to 2012 was acquired from the University of Washington's Polar Science Center and is derived using the Pan-Arctic Ice Ocean Modeling and Assimilation System (PIOMAS) (Zhang & Rothrock, 2003) (http://psc.apl.washington.edu/wordpress/research/projects/arctic-sea-ice-volume-anomaly/, 2013-04-26). The PIOMAS model assimilates sea ice concentration measurements from the NSIDC, SST from NCEP, and atmospheric variables from NCEP reanalysis, which are based on in situ and satellite derived measurements, to produce a sea ice volume index. The PIOMAS results have been validated with submarine observations, and data from oceanic moorings and remote sensing. For monthly data, the uncertainty is an order of magnitude smaller than the sea ice volume (Schweiger et al., 2011).

2.2.7 Snow cover extent

Monthly SCE for North America and Eurasia (1979-2012) was calculated from the NOAA snow chart climate data record produced by Rutgers University Global Snow Lab (http://climate.rutgers.edu/snowcover/, 2013-07-06). The complete SCE record combines the NOAA snow charts from 1967-1999 with remote sensing derived SCE from 1999-2012 (Helfrich et al., 2007). To avoid missing data in several summers prior to 1979 and to maintain consistency with sea ice extent and volume observations, only SCE observations from 1979-2012 are used. Spring SCE for both the Eurasian and North American Arctic, derived from the NOAA snow charts climate data record, has been shown to agree well with other independent SCE data sets and has been used to quantify cryospheric changes linked to atmospheric warming and circulation variability (Brown et al., 2010; Derksen & Brown, 2012).

16

2.3 Methods

2.3.1 Self-organizing maps

The SOM method is a neural network tool that applies an unsupervised training algorithm to produce a series of non-linear, topologically organized nodes, each with a reference vectors that represent a lower dimensionality version of the input data (Kohonen, 2001; Kohonen, 2013). For climatological studies, SOM provides a method akin to clustering that reduces spatially and temporally large gridded data sets into a specified number of output patterns that describe the range and frequency of observed input patterns (Hewiston and Crane, 2002; Cassano et al., 2006; Reusch et al., 2007; Reusch, 2010). For the analysis of extreme/rare events and/or systematic changes, the SOM provides an advantage over traditional clustering methods such as principal components (PC) analysis and empirical orthogonal function (EOF) analysis as its non-linear outputs have the capability to classify rare events or new system regimes and account for them in a probability analysis (Reusch et al., 2005; Reusch, 2010). Thus, the SOM provides a robust tool for identifying extreme events and systematic shifts in GPH anomalies observed in the Arctic since 2007.

A SOM consists of an array of nodes, the quantity of which is defined by the user. Each node has a unique reference vector that represents a generalized pattern of the input data. When SOM training is complete, the reference vectors found across the array of nodes describe the range of patterns found in the input data.

In the first step of SOM training, a reference vector is created for each node. These reference vectors have the same dimensions as the input data vectors and represent a first approximation of the range of patterns present in the input data based on the first two eigenvectors (Kohonen, 2001 and 2013). The batch SOM training algorithm iterates through the training steps, repeatedly presenting the input data vectors to the reference vectors. At each iteration, the best matching reference vector is chosen for each of the

input vectors based on Euclidian distance, and the reference vectors are then modified to more closely match the input vectors. Additionally, based on the neighbourhood size, the neighbouring node's reference vectors are, to a lesser degree, modified to match the input vector. This has the effect of grouping similar patterns in adjacent nodes, and displacing the two most dissimilar patterns to opposite corners of the final SOM. Through the batch training process, the reference vectors are incrementally modified to represent the span of the input data and the neighbourhood window maintains topological continuity between reference vectors. This batch training method (where multiple input vectors are presented to the SOM at each iteration) is preferred over the single vector training method (one input vector per iteration is presented to the SOM) because it is more mathematically stable (no user defined learning rate) and computationally efficient (Kohonen, 2001; Reusch, 2010).

Developing a SOM requires user defined parameters for the number of training steps, neighbourhood size, grid topology and grid dimensions. Detailed descriptions of these parameters and considerations for selecting appropriate values are provided in Kohonen (2001), Hewitson and Crane (2002), Cassano et al. (2006), Reusch et al. (2007), Reusch (2010) and Kohonen (2013). Briefly, the number of training steps prescribes the number of times the input data are presented to the reference vectors and the generalized patterns are updated. The neighbourhood size prescribes the number of nodes surrounding the best matching node that are modified at each iteration. The grid topology defines the layout of the nodes (hexagonal vs. square grid) and the grid dimensions lay out the number of rows and columns of nodes. The hexagonal grid is preferred to a rectangular grid because it maximizes the number of connections between a node and its neighbours (Kohonen, 2001; Kohonen, 2013). Selecting the appropriate number of nodes for a SOM is a subjective decision. The smaller the number of nodes, the more generalized each pattern becomes. However, this also increases the difference between an input pattern and its best matching node.

Conversely, a large number of nodes begins to erode the benefits gained by reducing the dimensionality of the input data. Finally, asymmetric dimensions are recommended to maintain network stability during training (Kohonen, 2001, Reusch et al. 2005).

As the user defined parameters (grid dimensions, training steps and neighbourhood size) can create the potential for poor representation of the input data during SOM training, and ultimately poor classifications of the input data (Kohonen, 2001; Reusch, 2010), it is advisable to train a number of SOM with varying parameters to evaluate the robustness of the final SOM (Cassano et al., 2006; Schuenemann & Cassano, 2010). To gauge the number of nodes required to describe the span of the input space, an EOF analysis was done. The first 30 and 42 EOFs accounted for 82% and 87% of the cumulative explained variance respectively. Above the first 42 EOF, additional increases of explained variance were minimal. Therefore, grid dimensions of 4x3, 5x6, 6x5, 5x7, 7x5, 6x7 and 7x6 were systematically evaluated with neighbourhood sizes of 1-4 and training steps from 200-2000. The difference in RMSE associated with all SOM variations was less than 3%. Chosen for its low RMSE and its ability to distinguish GPH patterns, the SOM master map presented here has five rows and six columns (5x6), a neighbourhood size of 3 and completed 400 training iterations.

2.3.2 Nodes of interest

The nodes of interest (NOI) are the SOM nodes that represent strong positive GPH anomalies over the Canadian Arctic and western Greenland. In each node, the mean area weighted GPH anomaly was calculated for the domain 65°N-85°N and 250°E-330°E (see Figure 2-1). The NOI identify the nodes where the mean area weighted GPH anomaly is greater than one standard deviation above the mean of the mean area weighted GPH anomalies. To show the monthly vertical profile of the NOI, Figure 2-2 shows the April to August 2007-2012 NCEP air temperature anomalies (a) and geopotential thickness (distance between pressure surfaces) anomalies (b) for the

domain 65°N-85°N and 250°E-330°E relative to the 1951-2010 climatology. Both air temperature anomalies and geopotential thickness anomalies share similar vertical and latitudinal patterns in all months, however, significant anomalies of air temperature and geopotential thickness occur only in June, July and August. The NOI generalized circulation patterns in June, July and August are consistent with circulation patterns reported in the literature that have promoted warm air advection into the CAA and maximized incoming shortwave radiation since 2007 (Overland et al., 2012; Gascon et al., 2013, Hanna et al., 2013).

2.4 Results

2.4.1 SOM master map

A 5x6 node SOM master map, producing 30 generalized patterns, was trained using 500 hPa GPH anomaly data from NCEP R1 and five CMIP5 models (Figure 2-3). The RMSEs of the daily 500 hPa GPH anomalies and the best matching node in the SOM for NCEP, BCC, CanESM2, CCSM4, MPI-ESM-LR and NorESM models are 41.1, 41.2, 39.4, 44.7, 42.8, 40.4 m respectively. The nodes in the upper right quadrant of the SOM represent generally negative GPH anomalies over western Greenland and the Canadian Arctic, while those in the upper left and lower right represent neutral anomalies. The lower left quadrant contains the NOI (nodes 1, 2, 7, 9 and 10) and represents generally strong positive GPH anomalies over western Greenland and the Canadian Arctic. With training and verification of the SOM complete, input data can be constrained by model (individual or ensemble) and/or by time to calculate the number of days that are represented by each node. If all circulation types occurred with an equal frequency, the frequency of every node would be 3.33%

2.4.2 NCEP and radiosonde geopotential height anomalies

The NCEP data set provides daily summer gridded, observationally constrained states of the 500 hPa GPH anomaly fields from 1948-2012. The frequency distribution of the

20

full NCEP data set (Figure 2-4) is statistically uniform across the SOM nodes with the exception of node 14, which occurs at a frequency greater than the 95% significance threshold determined by the frequency of all nodes. The cumulative frequency of the NOI representing strong positive GPH anomalies over the CAA and western Greenland between 1948 and 2012 is 15.7%.

The increasing frequency of positive GPH anomalies since 2007 reported in the literature (Sharp et al., 2011; Overland et al, 2012, Fettweis et al., 2013; Gascon et al., 2013; Tedesco et al., 2013) provides a valuable starting point to evaluate the capabilities of the SOM. Figure 2-5 shows the frequency distribution of GPH patterns from NCEP for 2007-2012. Evident in the frequency plot is the strong rise in frequency above the 95% confidence level at nodes 2, 4, 7, 9, 10, 14 and 17. The mean cumulative frequency for the NOI rose from 13.6% for 1948-2006 to 36.2% for 2007-2012, meaning that strong positive GPH anomalies over the CAA and western Greenland occurred 2.7 times more often between 2007 and 2012 than during the 1948-2006 period. As an example of such an anomaly, a warm high pressure ridge over the Greenland ice sheet was a significant driver of the extreme melt event on July 12, 2012 (Nghiem et al, 2012; Hanna et al., 2013; Tedesco et al., 2013). Using the SOM, the strengthening and weakening of a high pressure ridge can be tracked in the 500 hPa GPH anomalies over the week preceding the melt event. On July 8-9th, the atmospheric state was described by node 7, for July 10-11th by node 10, and for July 12-15th by node 17. The importance of the NOI for ice cap/sheet melt is evident as the four days preceding the melt event fell within the NOI.

Prior to 2007, the last anomalously warm period within the instrumental record in the CAA occurred in the late 1950s and early 1960s (Fisher et al., 2012; Zdanowicz et al., 2012). Alt (1978; 1979; 1987) classified synoptic patterns in the CAA during this period and compared them with observed glacier mass balance. Particular interest was paid to

high pressure events in 1962 and 1963 that resulted in anomalously negative mass balances. Figure 2-6 shows the frequency of occurrence of high pressure events for 1957-1963. The occurrence of nodes 2, 4, 8 and 21 was greater than expected with a 95% confidence window, and the cumulative NOI frequency was 20.3%. Node 2 is the only significant node within the NOI, although node 4 also represents positive GPH anomalies over the western Arctic. While the frequency distribution for the 1957-1963 period shows differences from the 2007-2012 period, it is evident that both periods share above average frequencies of positive GPH anomalies over the CAA and western Greenland. To evaluate variability in the frequency of strong positive 500 hPa GPH anomalies from 1948-2012, the annual summer frequency for the NOI and its five year running mean are shown in Figure 2-7. The horizontal dashed line represents two standard deviations above the mean frequency. In general, higher frequencies are observed prior to 1963 than from the mid-1960s to the mid-1990s. There is a gradual rise in frequency from the mid-1990s to the mid-2000s prior to the sharp rise between 2007 and 2012. In the later period, the frequency of high pressure events exceeds the mean by more than two standard deviations in four individual years, as does the five year running mean.

To ensure that the rise in frequency of positive 500 hPa GPH anomalies found in NCEP since 2007 has not resulted from poor data assimilation during the reanalysis process, the frequencies of strong positive 500 GPH anomalies in upper air soundings made at Alert, Resolute and Aasiaat are shown in Figure 2-8. At Alert and Resolute, nearly identical trends are found, where higher frequencies occur in the 1950s and early 1960s, then lower frequencies through the 1970s and 1980s and very high frequencies beginning in 2007. As the Aasiaat record begins in 1964, it misses the earlier period of high frequencies of positive 500 hPa GPH anomalies, but shows low frequency variability through the 1970s and 1980s and a very strong increase in frequency after

2007. At all three sites, the sharp increase in frequency after 2007 drove the five year running mean more than two standard deviations above the mean.

Both NCEP reanalysis data and radiosonde measurements show that there has been a significant increase in the frequency of positive summer GPH anomalies over the CAA and western Greenland since 2007. It would therefore be expected that the persistence of positive GPH anomalies might also have increased. The SOM provides the opportunity to calculate the number of consecutive days for which a system persists within each node, or group of nodes. Over the period 1948-2012, the mean duration of periods of consecutive days characterized by NOI was 4.0 ±1.9. Therefore, systems that last 6 days or more can be viewed as quasi-stationary anticyclonic systems, rather than as transient anticyclonic systems. Figure 2-9 shows the number of systems per summer that reside in the NOI for 6 days or more. Most years have only one anticyclonic system that resides over the NOI for 6 or more days. However, the number of 6+ day periods with strong positive 500 hPa GPH anomalies has risen to 2 or 3 per summer since 2007 and the five year running mean has risen to 2.6. This is a statistically significant change at the 95% confidence level. As causal relationships have been established between anticyclonic weather systems, surface air temperature measurements and the SMB of glaciers and ice caps in the High Arctic (Alt, 1987; Gascon et al., 2012; Hanna et al., 2013), statistically significant correlations should exist between the NOI frequency index (Figure 2-7), surface temperature measurements, and SMB measurements in the CAA and on the west coast of Greenland.

2.4.3 Surface air temperature anomalies

Mean summer surface air temperature anomalies for 1948-2012 are available for five sites in the CAA (Alert, Coral Harbour, Cambridge Bay, Eureka and Resolute) and three sites on the west coast of Greenland (Upernavik, Ilulissat and Nuuk). The spatial distribution of these locations provides good latitudinal (64.2°N-82.5°N) and longitudinal

(74.9°W-128.9°W) coverage (see Figure 2-1). The correlation coefficients for the frequency of strong positive GPH anomalies and mean summer air temperature anomalies are listed in Table 2-1. Very strong and significant ($p<0.01$) correlations (>0.70) are found for Resolute and Eureka and strong (0.53-0.69) and significant ($p<0.01$) correlations are found for the three sites on Greenland (Upernavik, Ilulissat, and Nuuk). A moderate significant correlation (0.45, $p<0.01$) was found for Alert, a weak significant correlation (0.30, $p<0.05$) was found for Coral Harbour and no significant correlation was found for Cambridge Bay. For each location, a cross-correlation analysis revealed no significant annual lags.

Since all the meteorological stations are located on or near the coast, the variability in the strength of the correlations provides some insight into the effect of anticyclonic systems over the region, particularly in the spring when the sea ice is still intact. Coral Harbour and Cambridge Bay are both located in the southwest of the domain used to calculate the NOI and an inspection of NOI GPH anomaly fields shows that these sites are located on the periphery of the positive anomalies. As Cambridge Bay and Coral Harbour are located 600 km and 1100 km south of Resolute respectively, sea ice break up would be expected to occur earlier than at Resolute and Eureka and local weather would thus become more affected by maritime climatic conditions earlier in the year. Similar sea ice conditions might be expected to apply to Upernavik, Ilulissat and Nuuk, as sea ice break-up in Baffin Bay is expected to occur earlier in the spring than from areas around Resolute and Eureka, allowing open water to become an important climatic influence. Based on the relationship between variations in surface air temperatures and the frequency of strong positive 500 hPa GPH anomalies over the CAA and western Greenland, it appears that surface air temperatures in the southwestern CAA have been minimally influenced by more frequent anticyclonic circulation, surface air temperatures on the west coast of Greenland have been strongly

influenced by more frequent anticyclonic circulation, and the strongest impact of more frequent anticyclonic circulation has been felt in the Canadian high Arctic.

2.4.4 Surface mass balance

The variation in annual SMB of glaciers and ice caps in the CAA has been shown to be governed largely by the intensity of summer melt (Oerlemans & Reichert, 2000; Braithwaite, 2005; Koerner, 2005). Since 2005, ice masses in the CAA have displayed a negative SMB trend (Figure 2-10). For June and July between 2005 and 2010, Gascon et al. (2013) found that, when positive 500 hPa GPH anomalies prevailed over the Devon Ice Cap, increased incoming shortwave radiation raised the total melt energy by as much as 24% above the monthly average. It is therefore expected that the NOI frequency index would be negatively correlated with SMB over the period from the 1960s to 2011. For the Devon Ice Cap, Meighen Ice Cap, Melville South Ice Cap and White Glacier, the correlation coefficients between the frequency of positive GPH anomalies and SMB are -0.62, -0.71, -0.54 and -0.70 respectively (all significant at $p<0.01$). The sign and magnitude of these coefficients are consistent with the results of Hanna et al. (2013), who correlated runoff from the Greenland Ice Sheet with the Greenland Blocking Index, a measure of the 500 hPa GPH over Greenland. The spatial pattern of the strengths of the correlations resembles that for the surface air temperatures, where Devon Ice Cap, Meighen Ice Cap and White Glacier, located near Resolute and Eureka show very strong correlations whereas Melville South Ice Cap, located outside the western boundary of the NOI domain, shows only a moderate correlation.

Given the evidence of the impact of positive summer GPH anomalies over the CAA on SMB in two different time periods (Alt, 1987; Gascon et al., 2013) and the very strong correlations that extend over the full observational record (1960s-2012), it is clear that the frequency of occurrence of positive 500 hPa GPH anomalies in summer is a major

control on the SMB of ice masses in the CAA. Therefore, it is critical to evaluate the ability of the current generation of climate models to predict the frequency of positive GPH anomalies over the CAA and western Greenland if they are going to be used to drive regional SMB projections.

2.4.5 CMIP5 geopotential height anomalies

As a metric to evaluate the capability of CMIP5 models to reproduce atmospheric circulation patterns in the Arctic, the RMSE calculated from the daily 500 hPa GPH anomaly fields and their best matching node and the frequency of occurrence of daily 500 hPa GPH anomalies over the full time domain (1950-2025) were calculated. Using RMSE from NCEP as the expected result, the percent differences in RMSE between NCEP and the BCC, CanESM2, CCSM4, MPI-ESM-LR and NorESM models are 0.3, -4.0, 8.8, 4.2, and -1.6 % respectively. When each model's daily 500 hPa GPH anomalies for 1950-2025 are classified by the SOM, the frequencies of occurrence for each node of the CanESM2 model fall within the range prescribed by the 95% significance level. Similar to NCEP, the BCC, CCSM4 and MPI-ESM-LR models each have one node that surpasses the 95% significance threshold and the NorESM model has one node below the 95% significance threshold. The cumulative frequency for the NOI from NCEP was 15.7%, compared to 10.9%, 12.2%, 19.4%, 11.4% and 16.5% for the BCC, CanESM2, CCSM4, MPI-ESM-LR and NorESM models respectively. Based on these results, it is reasonable to conclude the five CMIP5 models are capable of reproducing the patterns and long term frequencies of occurrence of 500 hPa GPH anomalies found in NCEP.

To evaluate trends in the annual frequency of positive 500 hPa GPH anomalies, plots similar to Figure 2-7 (using NCEP) were prepared for each of the CMIP5 models (Figure 2-11). While the mean NOI frequency for each model is similar to NCEP, no model produces a significant change in the frequency of occurrence of 500 hPa GPH

anomalies through the period 1950-2025. More significantly, no model produces consecutive years where the NOI frequency exceeds two standard deviations of the mean, or generates a five year running mean that surpasses the 95% threshold.

In the NCEP NOI frequency time series, the 2007-2012 period is the most striking anomaly. To quantify the magnitude of the rate of change, the slopes of linear regressions of the NOI frequency from 1970-2012 for NCEP and 1970-2012 and 1970-2025 for the CMIP5 models are shown in Table 2-2. The magnitude of the slope for NCEP (0.48) is twice that of the closest CMIP5 model (0.24 for CanESM2), and over 4 times as large as for the remaining models. While it is premature to call the frequency of positive GPH anomalies since 2007 a long term trend that signals a systematic shift in Arctic atmospheric circulation, the rate and magnitude of the recent changes are not reproduced by a number of the most recent generation of CGCMs (Belleflamme et al., 2012; Overland et al., 2012; Hanna et al., 2013).

2.4.6 Potential drivers of positive 500 hPa geopotential height anomalies

Overland et al. (2012) argued that increased meridional heat advection and decreasing Northern Hemisphere snow cover extent should be, at least in part, responsible for the persistent anticyclonic conditions that have been observed in June over Greenland and the CAA since 2007. In addition to these factors, the reductions in the extent and thickness of Arctic sea ice since 2007 are likely to have impacted atmospheric circulation in the Arctic (Serreze & Barry, 2011; Francis and Vavrus, 2012; Screen et al. 2012). To test the relative importance of meridional heat advection, changes in snow cover extent, sea ice extent and sea ice volume, a series of correlations were made with the NCEP NOI frequency index (Figure 2-7). Correlations between the NOI frequency index and times series of eddy heat flux, SCE, sea ice extent and sea ice volume were calculated for each month from April to August. This was done to examine potential lags between the drivers and the response of GPH anomalies. The one exception to this is

the correlation between the AMO index and NOI frequency index. The AMO is better expressed as a summer average due to its multidecadal time scale.

2.4.7 Meridional heat advection

To quantify the atmospheric meridional heat advection into Baffin Bay and the CAA, the monthly 500 hPa NCEP area weighted mean eddy heat flux was calculated for the domain 65°N-85°N and 250°E-330°E. Correlations between the eddy heat flux and NOI frequency index are shown in Table 2-3a. The correlation coefficients for April, May, July and August are $<\pm0.18$ and not significant at $p<0.05$. For June, the correlation coefficient is 0.32 and significant at $p<0.01$.

North Atlantic SST variability, described by the AMO index, has been shown to co-vary with air temperature measurements in Greenland and CAA, and with ice melt/runoff from Greenland (Chylek et al., 2009; Hanna et al., 2013). For the ice caps in the CAA, correlations between SMB measurements and the AMO index that are significant at $p<0.02$ are found for the Meighen (-0.32) and Melville South Ice Cap (-0.36), while correlations that are significant at $p<0.01$ are found for the White Glacier (-0.36) and Devon Ice Cap (-0.56). This suggests that anomalously warm North Atlantic SST are related to positive surface air temperature anomalies and increasing SMB losses in the western Arctic, but no mechanism has been suggested to account for these relationships. Using the AMO index and the NOI frequency index, the correlation between North Atlantic SST and the frequency of positive 500 hPa GPH anomalies is 0.41 ($p<0.01$), indicating that there appears to be a moderately positive relationship between the frequency of positive 500 hPa GPH anomalies and North Atlantic SST variability.

2.4.8 Sea Ice extent and sea ice volume

Arctic waters are a large source of heat to the higher latitudes, and are continuing to warm with SST anomalies exceeding 5°C in the Eastern Arctic Ocean in 2007 (Steele et al., 2008; Blüdgeon et al., 2012; Screen & Simmonds, 2012). According to the NSIDC sea ice index, the sea ice extent in September declined by 13% per decade from 1979 to 2012, but only by 5% in April and May (Figure 2-12a). For the same period of time, PIOMAS sea ice volume decreased by 28% in September, 23% in April and 25% in May (Figure 2-12b).

To evaluate the relationship between sea ice extent and volume and the frequency of positive 500 hPa GPH anomalies, correlations were made between the NOI frequency index and the monthly NSIDC sea ice index and the PIOMAS sea ice volume index for April to August. In June, July and August, correlations between sea ice extent and the NOI frequency index are -0.61, -0.73 and -0.74 respectively and significant ($p<0.01$) (Table 2-3b). Similar results are found with correlations between the sea ice volume and the NOI frequency index where the correlation coefficients for June, July and August are all statistically significant ($p<0.01$) and increase from -0.70 in June to -0.74 in August (Table 2-3c). The notable differences between the sea ice extent and sea ice volume indices are found in April and May, when there are no statistically significant correlations between sea ice extent and the NOI frequency index, but correlation coefficients between sea ice volume and the NOI frequency index are -0.64 and -0.66 ($p<0.01$). As the PIOMOS sea ice volume is derived by assimilating the NSIDC sea ice extent, the differences should primarily reflect changes in sea ice thickness. Therefore, it is possible that the decline in pan-Arctic sea thickness in April and May is a more important metric than sea ice extent when evaluating the evolution of positive 500 hPa GPH anomalies over the CAA and western Greenland.

2.4.9 Snow cover extent

Snow cover plays a significant role in the surface energy balance of the Arctic through its influence on surface albedo and energy fluxes (Walsh & Chapman, 1990; Foster et al., 2013). While numerous studies have used spring Northern Hemisphere SCE (Figure 2-12c) as a metric for global climate change (Brown & Braaten, 1998; Brown et al., 2010; Frei & Lee, 2010; Derksen & Brown, 2012), very little work has looked directly at the feedback between declining spring/summer SCE and summer atmosphere circulation. Using the same approach described in the sea ice section, correlations were made between the frequency of positive GPH anomalies and monthly SCE for North America and Eurasia from April to August (Table 2-3d). For North America, significant correlations of -0.35 ($p < 0.05$), -0.54 ($p < 0.01$) and -0.44 ($p < 0.01$) were found for May, June and July respectively. For Eurasia, correlations of -0.45, -0.59, -0.56, -0.56, -0.44 and significant to $p < 0.01$ were found for April, May, June, July and August respectively.

2.4.10 Multiple linear regression models

Monthly correlations between the NOI frequency index, sea ice extent, sea ice volume, SCE and meridional heat advection found statistically significant relationships in one or more months for each time series. To compare the relative significance of each time series by month, a multiple linear regression model was developed for each month between April and August. Sea ice extent, sea ice volume, Northern Hemisphere SCE and eddy heat flux time series were standardized and used as the independent variables in the regression models. The NOI frequency index was also standardized and used as the dependent variable. Standardization allows for the direct comparison of coefficients within each model. To reduce the number of independent variables in the regression model (increasing the statistical significance of the model), North American and Eurasian SCE are replaced with the Northern Hemisphere SCE. To test for multicollinearity between the independent variables, the Durbin-Watson statistic is calculated for each multiple linear regression model. The results indicate statistically significant multicollinearities exist in all months. Therefore, the multiple linear regression

models are only considered significant when the Variance Inflation Factor (VIF), a measure of the influence of multicollinearity on the regression coefficients, is less than 10.

The R^2 and standardized coefficients are presented for each multiple regression model in Table 2-4. The R^2, an estimate of the portion of variance in the NOI frequency index explained by sea ice extent, sea ice volume, Northern Hemisphere SCE and eddy heat flux, ranges from 0.57 to 0.60 or 57% to 60%. Based on the F-test for each month, all five models are significant at $p<0.01$. Within each model, the standardized coefficients (in units of standard deviation) rate the relative importance of each independent variable. Statistical significance of the standardized coefficients was tested using a Student's t-test. For April and May, the only statistically significant ($p<0.01$) independent variables are sea ice extent and sea ice volume. The standardized coefficient of sea ice extent is positive, indicating that an increase in sea ice extent would result in an increase in the frequency of anticyclonic circulation over Greenland and the CAA, whereas the standardized coefficient for sea ice volume indicates a strong negative relationship. In June, sea ice volume and eddy heat flux are the only two statistically significant independent variables. The magnitude of the coefficients indicates that influence of sea ice volume is approximately two times greater than that of eddy heat flux, and the sign of the coefficients indicates that decreasing sea ice volume and increasing eddy heat flux in June result in more frequent anticyclonic circulation over western Greenland and the CAA. The multiple regression models for July and August continue to explain 57% and 59% of NOI frequency variability respectively (significant at $p<0.01$), but there are no statistically significant ($p<0.05$) independent variables.

2.5 Discussion

A SOM was trained using daily summer 500 hPa GPH anomalies from NCEP (1948-2012) and five CMIP5 climate models (1950-2025). Five of the SOM nodes (the NOI)

have generalized patterns that represent strong positive 500 hPa GPH anomalies over western Greenland and the CAA and are consistent with anomalous atmospheric circulation patterns that have been shown to result in large SMB losses from glaciers and ice caps in the CAA in the early 1960s and from 2005-2010 (Alt, 1978 & 1987; Gascon et al., 2013). The annual cumulative frequencies of the NOI show considerable interannual variability, with generally higher frequencies of positive 500 hPa GPH anomalies in the late 1950s and early 1960s, comparatively lower frequencies in the 1970s and 1980s and a gradual rise in frequencies from the early 1990s to 2007 (Figure 2-7). Between 2007 and 2012, the frequency of positive 500 hPa GPH anomalies remained well above the climatological mean and surpassed two standard deviations above the mean in four of the six years. In addition to the rise in frequency of positive 500 hPa GPH anomalies, the number of persistent anticyclonic systems lasting six or more days tripled from 0.7 for 1948-2012 to 2.3 for 2007-2012. Based on the annual frequency and persistence of 500 hPa GPH anomalies between 1948 and 2012 it is reasonable to conclude that, while the period from the 1950s to early 1960s also shows above average anticyclonic circulation behaviour, the period from 2007 to 2012 is atypical in the 65 year record.

Strong and significant ($p<0.01$) correlations were found between the frequency of positive 500 hPa GPH anomalies and glacier SMB on the Devon Ice Cap (-0.62), Meighen Ice Cap (-0.71), Melville South Ice Cap (-0.54) and the White Glacier (-0.70). Correlations between surface air temperature and the NOI frequency index found significant ($p<0.01$) moderate to strong relationships (0.45 to 0.71) at all sites on Greenland and at Alert, Eureka and Resolute in the CAA. For Coral Harbour in the CAA, the correlation coefficient was weak, though significant (0.30, $p<0.05$) and the correlations for Cambridge Bay were insignificant. Alt (1978, 1979 & 1987) and Gascon et al. (2013) found anticyclonic conditions raised air temperatures, increased melt energy, and resulted in more negative SMB over relatively short periods of time (≤10

years). The strong relationship found between glacier SMB and the frequency of positive 500 hPa GPH anomalies suggests that anticyclonic circulation patterns in the western Arctic have been an important driver of summer melt in the CAA and therefore an important control on glacier SMB from the early 1960s through to 2012.

Considering that the CAA emerged as a the principal non-ice sheet source of eustatic sea level rise in the mid-2000s (Gardner et al., 2011 & 2013) and summer atmospheric circulation is an important control on glacier SMB in the CAA, testing the ability of global climate models to accurately replicate the spatial and temporal patterns of Arctic circulation is critical for producing robust surface mass balance and sea level projections. While the CMIP5 models were capable of reproducing the range and frequency of patterns found in NCEP over the full time domain (1950-2025), none replicated the magnitude of the anomalous high frequency of 500 hPa GPH anomalies found in NCEP between 2007 and 2012, despite having the time domain extended to the year 2025. Even if the frequency of anticyclonic circulation events from 2007 to 2012 is an extreme anomaly, its impacts will likely have a legacy in the Arctic climate system due to feedbacks such as the resulting decrease in ice surface albedo (Box et al., 2012). Modelled climate data used to drive glacier SMB models should include both the long-term spatial and temporal trends of anticyclonic circulation as well as the extreme events that are not currently captured in the CMIP5 models. Therefore, current projections of SMB losses driven by CMIP5 models will likely underestimate the Arctic Glacier and Greenland Ice Sheet contributions to eustatic sea level rise, particularly if the frequency of positive GPH anomalies remains at levels observed in NCEP since 2007 (Hanna et al., 2013; Lenaerts et al., 2013).

While the impacts of more frequent and persistent anticyclonic circulation anomalies are understood, pinpointing the driver(s) responsible for the sudden shift has remained challenging (Overland et al., 2012; Screen et al., 2012). To create the GPH anomalies

observed in the NCEP record between 2007 and 2012, additional thermal energy should have been added to the Arctic atmosphere. A number of potential physical changes have been suggested as mechanisms for this including increased meridional heat advection, decreasing sea ice extent, sea ice volume and spring Northern Hemisphere SCE (Serreze & Barry, 2011; Francis & Vavrus, 2012; Overland et al., 2012; Screen et al. 2012). To test the relative importance of these suggested physical changes, a series of correlations and a multiple linear regression analysis were carried out on a month to month basis between the observed physical changes and the NOI frequency index.

A summary of the results of correlations between the NOI frequency index sea ice extent and volume, Northern Hemisphere SCE and eddy heat flux is presented in Table 2-3. The eddy heat flux is only significant in June (0.32). Sea ice extent is not significant in April and May, but is significant in June, July and August (-0.61 to -0.74), whereas, sea ice volume is significant for April to August (-0.64 to -0.74). North American SCE is not significant in April and August, but is significant in May, June and July (-0.35 to -0.54), while Eurasian SCE is significant from April to August (-0.44 to -0.59). Multiple linear regression models were used to further evaluate the ability of sea ice extent, sea ice volume, Northern Hemisphere SCE and eddy heat flux to predict the NOI frequency index (see Table 2-4). For April to August, sea ice extent, sea ice volume, Northern Hemisphere SCE and eddy heat flux can explain 57% to 60% of the NOI frequency index variability. In April and May, sea ice volume was found to be the most important predictor of anticyclonic circulation incidence over western Greenland and the CAA. In June, sea ice volume remained the most important predictor, but meridional heat advection was also statistically significant. In July and August, sea ice extent, sea ice volume, Northern Hemisphere SCE and eddy heat flux were unable to predict the NOI frequency index with statistical significance. Therefore, it appears that the influence of meridional heat advection is only significant in June, sea ice volume is a more

significant influence than sea ice extent, and Eurasian SCE is a more significant influence then North American SCE for the development of the positive GPH anomalies that have been observed over western Greenland and the CAA since 2007. Based on these results, we hypothesize that an ensemble of Arctic feedbacks is primarily responsible for the observed rise in frequency and persistence of anticyclonic circulation over western Greenland and the CAA since 2007.

A schematic of the hypothesized feedback ensemble (Figure 2-13) incorporates three sources of increased thermal energy advection into the Arctic atmosphere, which has raised GPH, and resulting in more negative SMB over glaciers and ice caps in the CAA. The first loop (on the left side of Figure 2-13) is similar to the standard sea ice-albedo feedback, but also includes the more significant, decrease in spring/early summer sea ice volume. A decrease in sea ice volume/thickness should increase the vertical heat flux from the ocean to the atmosphere (assuming there is no significant increase in spring snowpack thickness (Screen & Simmons, 2012)), and would raise air temperatures and GPH. Greater GPH (more frequent anticyclonic circulation) would, in addition to increasing the meridional heat transport, result in more clear sky days, intensifying the surface incident shortwave radiation and enhancing the sea ice-albedo feedback. The right side of Figure 2-13 represents a terrestrial feedback similar to the left side of Figure 2-13. Here, decreased spring/early summer SCE results in lower albedo at the surface, increased energy absorption at the earth-atmosphere interface, and increased air temperatures. Increased air temperatures result in greater GPH, promote more anticyclonic circulation and reduced cloud cover, maximizing surface incident shortwave radiation and further decreasing SCE. The third source of heat into the Arctic, advected meridional heat, is not shown as a loop in Figure 2-13 because it is only significant in June. However, it may provide a pulse of heat in the spring/early summer, pushing the dominant circulation pattern past a threshold and into a new circulation regime that was not observed prior to 2007. Alternatively, it is possible that

35

the increase in meridional heat advection is the result of, rather than the cause of positive geopotential height anomalies. Determining if meridional heat advection is the response to, or driver of positive GPH anomalies is not possible with the temporal resolution of data sets and statistical methods used in this study.

Research into summer atmospheric circulation over the CAA is sparse; however, research focusing specifically on atmospheric circulation over the Greenland Ice Sheet is more plentiful and provides valuable comparison. Hanna et al. (2013) looked in detail at the atmospheric circulation associated with the July 2012 Greenland melt event using a combination of meteorological measurements, climate reanalysis, and regional climate modeling. Based on a sensitivity analysis of the regional climate model and in situ oceanic measurements, they concluded that sea ice extent and SST off the southwest coast of Greenland had little impact on the melt event, while warm air advected onto the ice sheet and lack of cloud cover (increased surface incident radiation) were the primary causes of the melt event. The increased frequency of positive GPH anomalies over Greenland has also been noted by Francis and Vavrus (2012), who looked at the connection between Arctic amplification (enhanced warming in the polar regions relative to the global average) and the position/amplitude of Rossby waves. Consistent with Rossby wave theory, Francis and Vavrus (2012) and Hanna et al. (2013) show that positive air temperature in the Arctic increased wave amplitudes and has resulted in slower westward propagation of the Rossby Waves and more frequent quasi-stationary anticyclonic circulation patterns.

The general consensus from the CAA and Greenland is that the statistically significant increase in the frequency of positive GPH anomalies (anticyclonic circulation) over the CAA and Greenland resulted in more negative glacier SMB between 2007 and 2012. What remains unclear is the relative influence of natural variability and anthropogenic forcings in the development of more frequent anticyclonic circulation since 2007. The

36

results presented here point to a complex set of connections and feedbacks that most likely include a combination of decreased sea ice volume (thickness), decreased SCE and increased meridional heat advection in the anomalously high frequency of positive GPH anomalies over Greenland and the CAA since 2007. As the CGCMs prepared for CMIP5 are unable to produce the observed trends in the frequency of positive GPH anomalies found in climate reanalysis, it remains unclear whether 2007-2012 is a period of exceptional natural variability, or the result of anthropogenically driven change in the Arctic.

2.6 Conclusions

Using the SOM algorithm, NCEP daily summer Northern Hemisphere 500 hPa GPH anomalies (1948-2012) were classified into thirty generalized atmospheric circulation patterns, five of which represent strong positive 500 hPa GPH anomalies over the CAA and western Greenland (NOI). The incident frequencies of the five patterns were used to create an NOI frequency index that describes the interannual variability in the frequency of anticyclonic circulation over the CAA and western Greenland between 1948 and 2012. The general trend in variability shows above average frequencies in the 1950s and early 1960s, below average frequencies in the 1970s and 1980s, a slow rise in frequencies between the 1990s and 2006, and then a statistically significant (above 95%) rise in frequencies from 2007 to 2012. The NOI frequency index is in good agreement with radiosonde measurements made at two meteorological stations in the CAA and one on the west coast of Greenland. Correlations between four 50 year glacier SMB records from the CAA, eight surface air temperature records from the CAA and west coast of Greenland, and the NOI frequency index produce strong and significant relationships between the frequency of anticyclonic circulation and surface melt/air temperatures above ~70°N in the CAA. These findings are consistent with previous work on the relationship between glacier mass balance and atmospheric circulation in the CAA (Alt, 1978; 1979; 1987; Gascon et al., 2013). The NOI frequency index was

compared with the frequencies of positive 500 hPa GPH anomalies over the CAA and western Greenland calculated from five CMIP5 models, the CMIP5 models were not capable of producing the sharp rise in frequency of positive 500 hPa GPH anomalies observed since 2007. This assessment is consistent with Overland et al. (2012) and Hanna et al. (2013).

To identify the likely sources of thermal energy into the Arctic that could be responsible for the trends found in the NOI frequency index and test the relative importance of each mechanism, the influences of meridional heat advection (eddy heat flux), Arctic sea ice extent, Arctic sea ice volume, North American SCE and Eurasian SCE were evaluated using a series of correlation and multiple linear regression analyses. For April to August, Arctic sea ice extent and volume, Northern Hemisphere SCE and meridional heat advection explained 57-60% of the NOI frequency index variability. In April and May, the strongest predictor of the frequency of anticyclonic circulation over western Greenland and the CAA was sea ice volume. In June, sea ice volume was still the most important predictor, however, meridional heat advection was also statistically significant. In July and August, the regression models explained 57% and 59% of the NOI frequency index variability respectively, however, sea ice extent, sea ice volume, Northern Hemisphere SCE and meridional heat advection were not individually statistically significant predictors.

Based on these results, we suggest that decreased spring snow cover extent and decreased sea ice volume (thickness) increase the vertical heat flux from the surface into the atmosphere, and increased the GPH in April, May and most notably June, July and August. As increased GPH in June promotes more cloud-free conditions, the radiative energy incident at the earth's surface is maximized, raising surface and air temperatures and further increasing GPH through July and August. With the addition of heat advected into the Arctic in June, these changes in heat fluxes could potentially

trigger the development of persistent GPH anomalies over the CAA and western Greenland. Significant positive GPH anomalies over Greenland increase the amplitude of the Rossby waves, slowing the propagation of anticyclonic systems (increasing the resident time of anticyclonic circulation regimes over the CAA and western Greenland) and increase the poleward advection of warm air into the Arctic (Francis and Vavrus, 2012; Hanna et al., 2013).

As the relationships identified here between GPH anomalies over the CAA and western Greenland, sea ice extent and volume, SCE and meridional heat flux presented here are statistical rather than causal, the suggested complex feedback is only hypothetical. To verify the roles of natural variability and anthropogenic forcings in the increase in frequency of 500 hPa GPH anomalies over the CAA and Greenland since 2007, CGCM capable of reproducing the observed frequency of atmospheric circulation patterns for the Arctic are required. In the meantime, the contribution of CAA glaciers and ice caps to forecasts of eustatic sea level rise based on CMIP5 data may need to be examined in more detail, particularly if the frequency of positive GPH anomalies remains at the levels observed between 2007 and 2012 (Hanna et al., 2013).

Weather Station	Corr. Coef.
Alert	**0.4519**
Cambridge Bay	0.20191
Coral Harbour	<u>0.30173</u>
Eureka	**0.71367**
Resolute Bay	**0.71055**
Upernavik	**0.61381**
Ilulissat	**0.53429**
Nuuk	**0.69088**

Table 2-1. Correlations coefficients between the frequency of strong positive 500 hPa GPH anomalies and mean summer air temperature anomalies on western Greenland and the CAA. Bolded values are significant at $p < 0.01$ and underline values are significant to $p < 0.05$.

Model	1970-2012	1970-2025
NCEP	0.48	
BCC	0.11	0.08
CanESM2	0.24	0.21
CCSM4	-0.05	-0.13
MPI-ESM-LR	0.09	0.23
NorESM	0.11	0.07

Table 2-2. Slopes from linear regressions of the NOI frequency for NCEP (1970-2012) and the CMIP5 models for 1970-2012 and 1970-2025.

Month	a) Eddy heat flux	b) Sea ice extent	c) Sea ice volume	d) Snow cover extent North American	Eurasia
Apr	-0.02	-0.22	**-0.64**	-0.06	**-0.45**
May	-0.01	-0.26	**-0.66**	_-0.35_	**-0.59**
Jun	**0.32**	**-0.61**	**-0.70**	**-0.54**	**-0.56**
Jul	0.17	**-0.73**	**-0.73**	**-0.44**	**-0.56**
Aug	0.18	**-0.74**	**-0.74**	-0.25	**-0.44**

Table 2-3. April to September monthly correlations coefficients between NSIDC sea ice extent, PIOMAS sea ice volume, and snow cover extent (North America and Eurasia) with the frequency of strong positive 500 hPa GPH anomalies identified using the NOI. Bolded values are significant at p<0.01 and underline values are significant to p<0.05.

Month	Overall model performance R^2	Sea ice extent Std. coef.	Sea ice volume Std. coef.	SCE Std. coef.	Eddy heat flux Std. coef.
April	**0.59**	**0.54**	**-1.02**	-0.10	0.21
May	**0.59**	**0.52**	**-0.88**	-0.23	0.03
June	**0.60**	0.26	**-0.71**	-0.15	**0.32**
July	**0.57**	-0.29	-0.48	-0.08	-0.20
August	**0.59**	-0.42	-0.28	-0.02	0.13

Table 2-4. R2 and standardized coefficients for monthly multiple linear regression models using standardized sea ice extent, sea ice volume, Northern Hemisphere SCE and eddy heat flux as the independent variables and standardized NOI frequency index as the dependent variable. Standardized coefficients are in units of standard deviation. Bolded values are significant at p<0.01 and VIF<10.
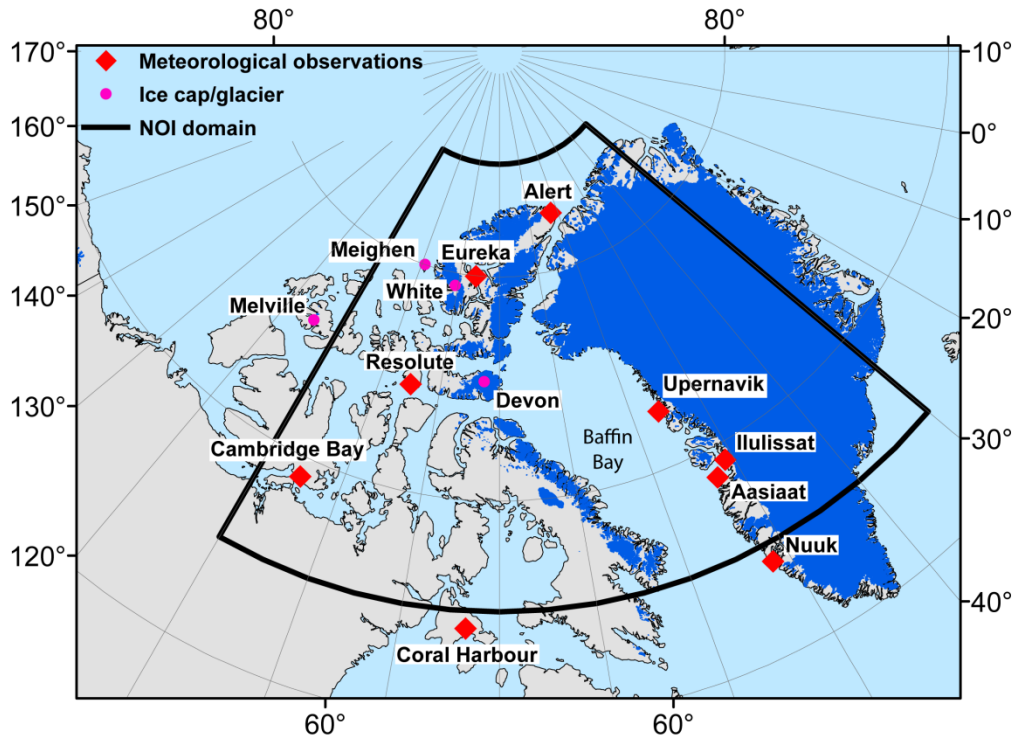
Figure 2-1. Site map for the CAA and Greenland with ice mass shown in dark blue. The black box indicates the bounds of the domain used to calculate the NOI on the SOM. Surface meteorological observations from stations at Alert, Coral Harbour, Cambridge Bay, Eureka, Resolute, Nuuk, Ilulissat and Upernavic and upper atmosphere meteorological observation stations at Resolute, Alert and Aasiaat are identified with red diamonds. The four long term surface mass balance records (Devon Ice Cap, Meighen Ice Cap, Melville Ice Cap and White Glacier) are shown with fuischia circles.
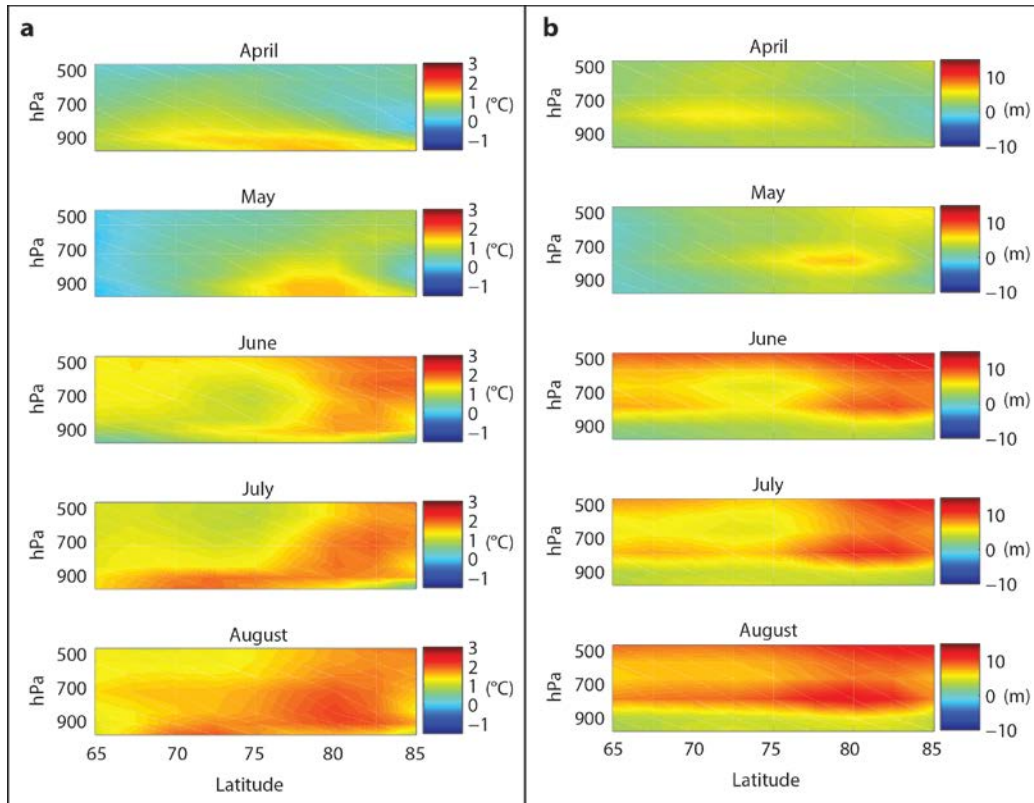
Figure 2-2. April to August 2007-2012 monthly vertical profiles of the NCEP air temperature anomalies (a) and geopotential thickness anomalies (b) for the CAA and western Greenland (65°N-85°N and 250°E-330°E) relative to the 1951-2010 climatology.

SOM Master Map
500 hPa geopotenial heigth anomalies (m) NCEP (1948-2012), CMIP5 (1950-2025) (Climatology 1951-2010)
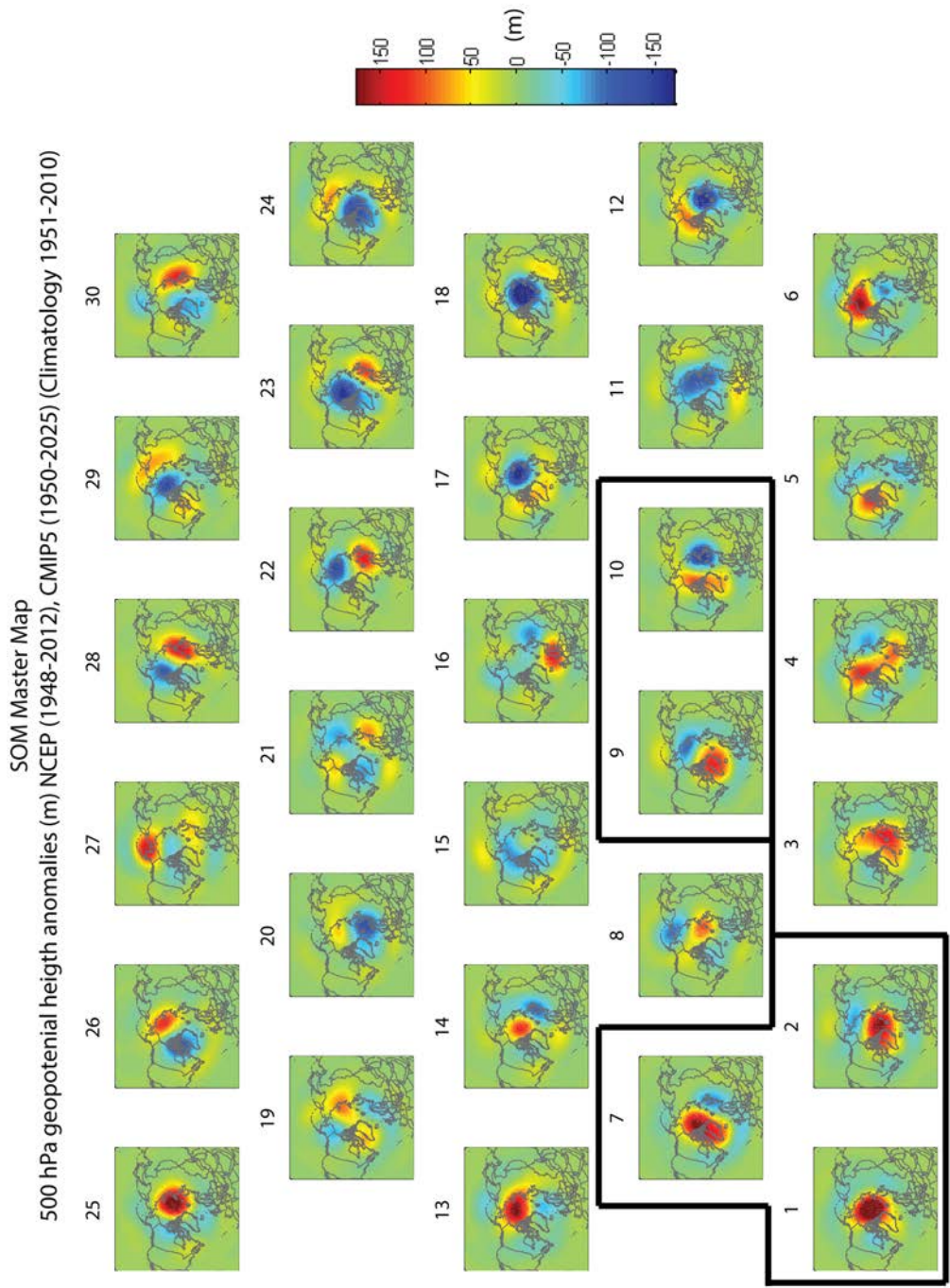
Figure 2-3. Master SOM. The NOI (1, 2, 7, 9, 10), representing strong positive geopotential height anomalies over the CAA and western Greenland are bounded by the black boxes.
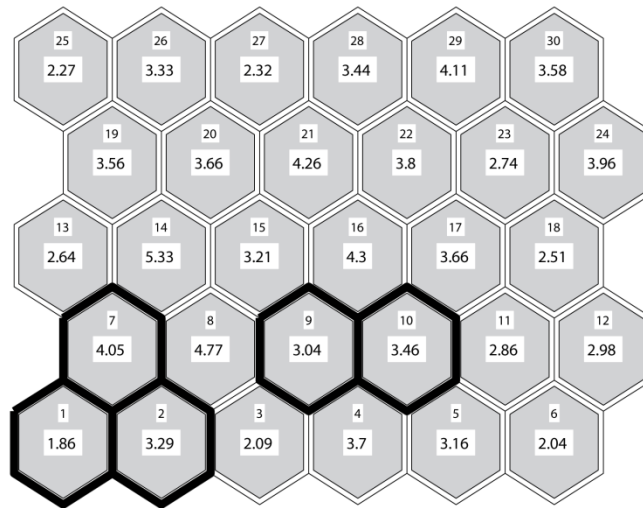
Cumulative frequency of highlighted area=15.7%

Figure 2-4. Frequencies of occurrences of 1948-2012 daily summer NCEP 500 hPa GPH anomalies classified by the master SOM. The NOI are outlined with black lines.
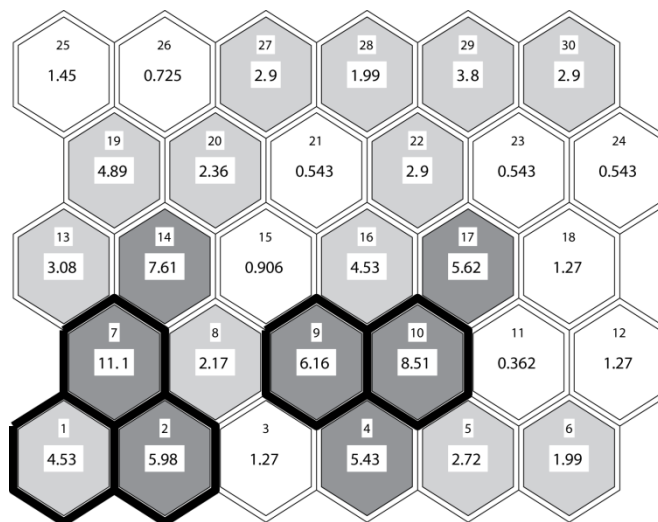
Cumulative frequency of highlighted area=36.23%

Figure 2-5. Frequencies of occurrences of 2007-2012 daily summer NCEP 500 hPa GPH anomalies classified by the master SOM. Light grey nodes have no statistically significant change in frequency, white notes have frequencies below the 95% significant threshold and dark grey nodes have frequencies above the 95% significance threshold.
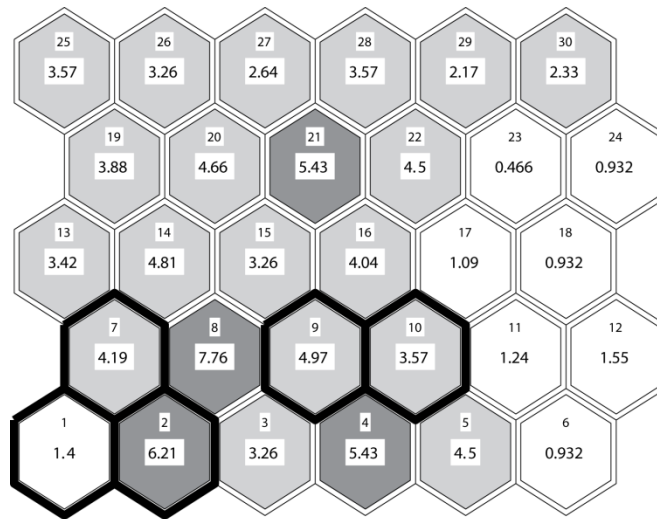
Cumulative frequency of highlighted area=20.34%

Figure 2-6. Frequencies of occurrences of 1957-1963 daily summer NCEP 500 hPa GPH anomalies classified by the master SOM. Light grey nodes have no statistically significant change in frequency, white notes have frequencies below the 95% significant threshold and dark grey nodes have frequencies above the 95% significance threshold.
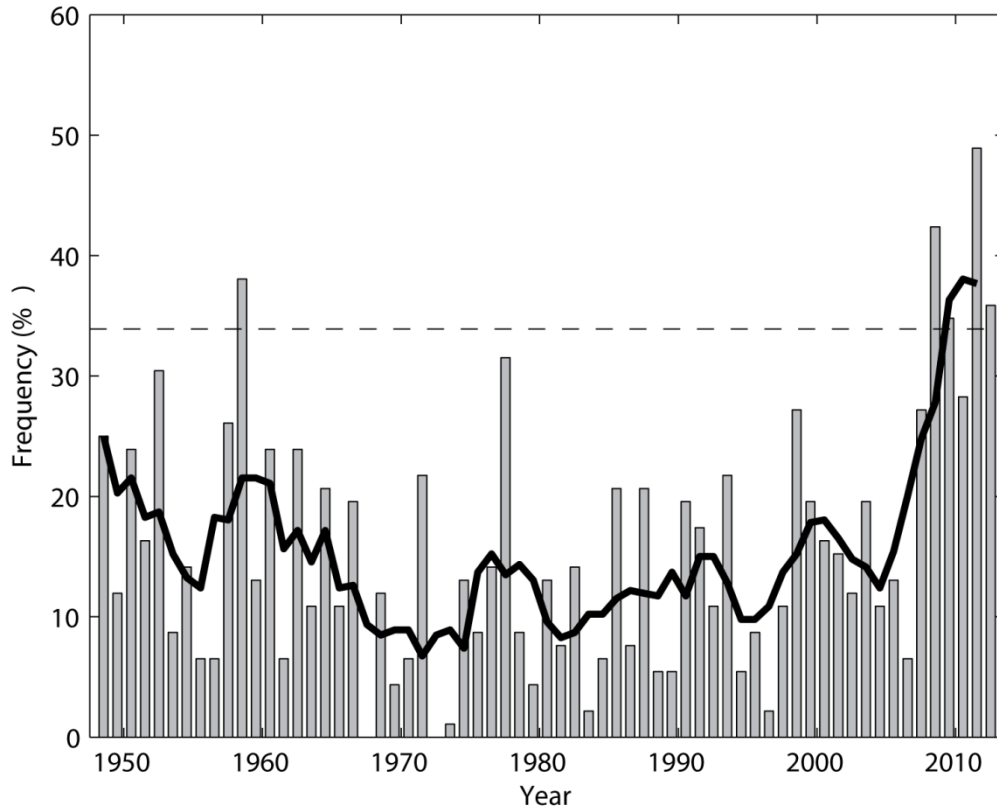
Figure 2-7. NCEP annual summer frequencies of strong positive 500 hPa GPH anomalies identified by the NOI. The solid line is the 5 year running mean and the horizontal dashed line marks two standard deviations above the climatological mean frequency.
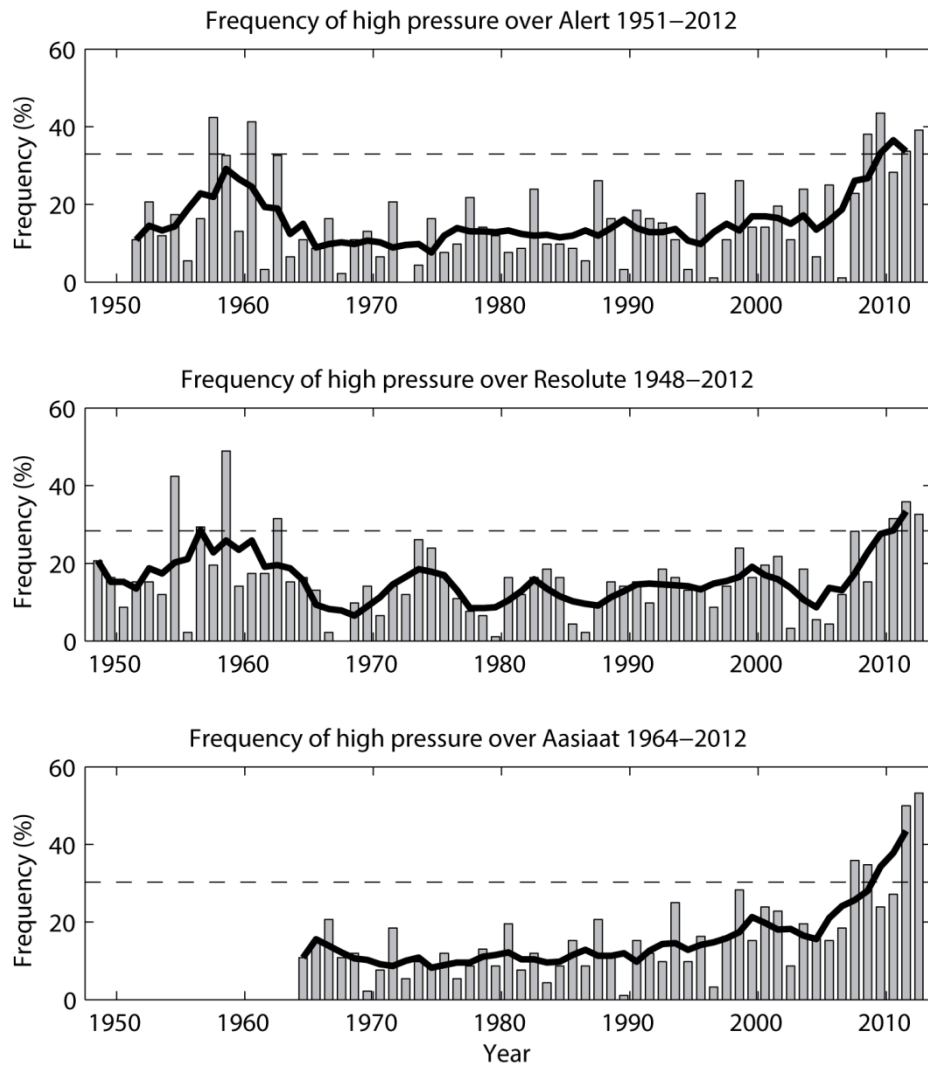
Figure 2-8. The bars represent the annual summer frequencies of strong positive GPH anomalies at three long running upper atmospheric meteorological stations. The solid line is the five year running mean and the horizontal dashed line marks two standard deviations above the climatological mean frequency.
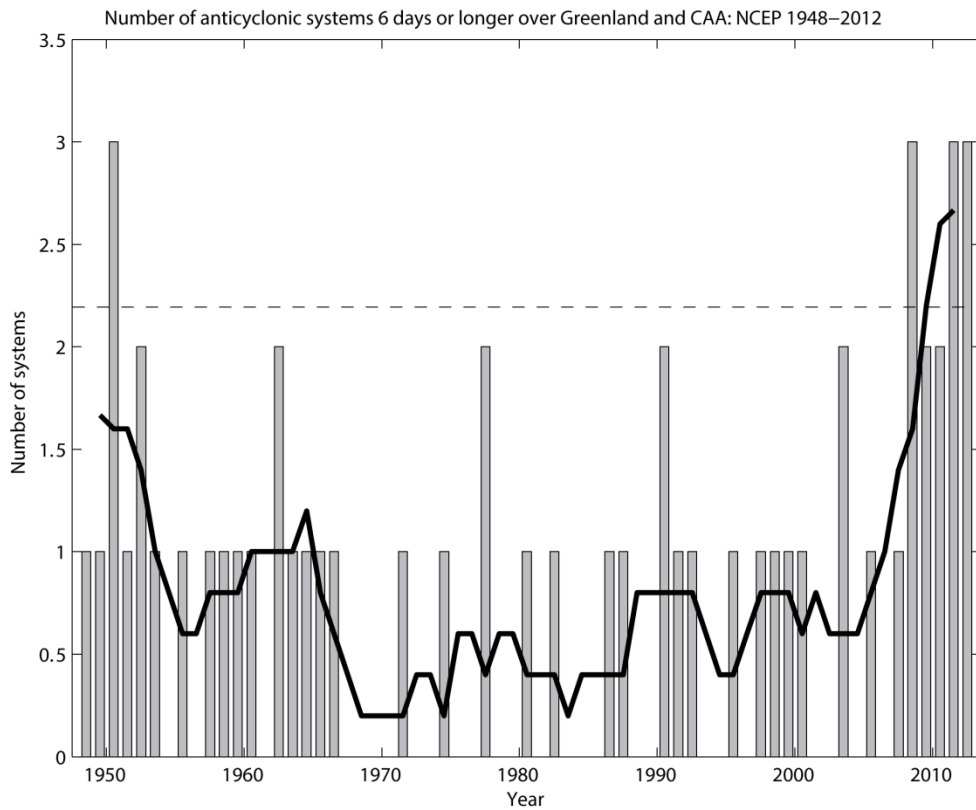
Figure 2-9. Using the NCEP record, the bars represent the number of 6 day or longer anticyclonic systems described by the NOI. The solid line is the 5 year running mean and the horizontal dashed line marks two standard deviations above the climatological mean frequency.
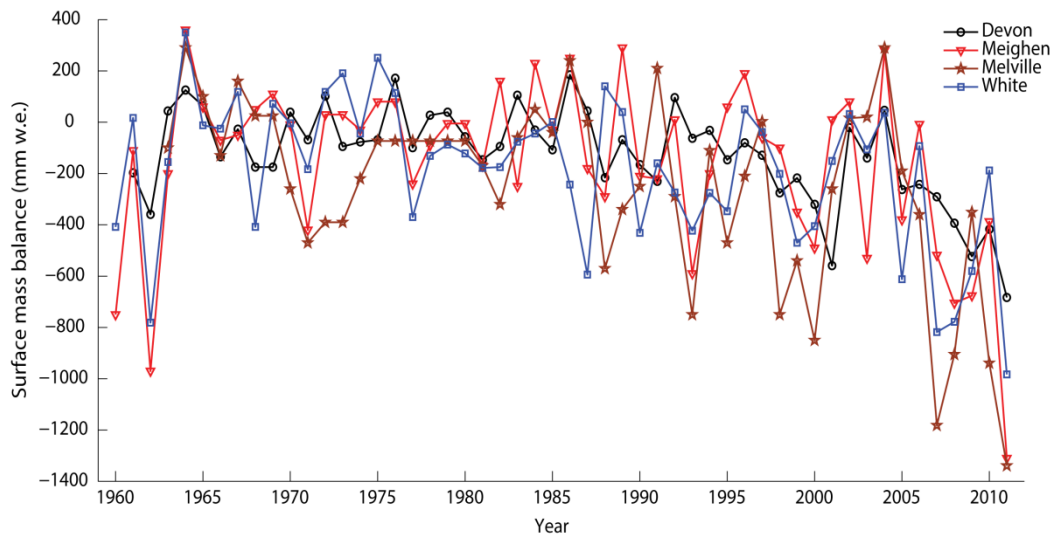
Figure 2-10. Annual SMB measurements for the Devon Ice Cap, Meighen Ice Cap, Melville Ice Cap, and White Glacier.
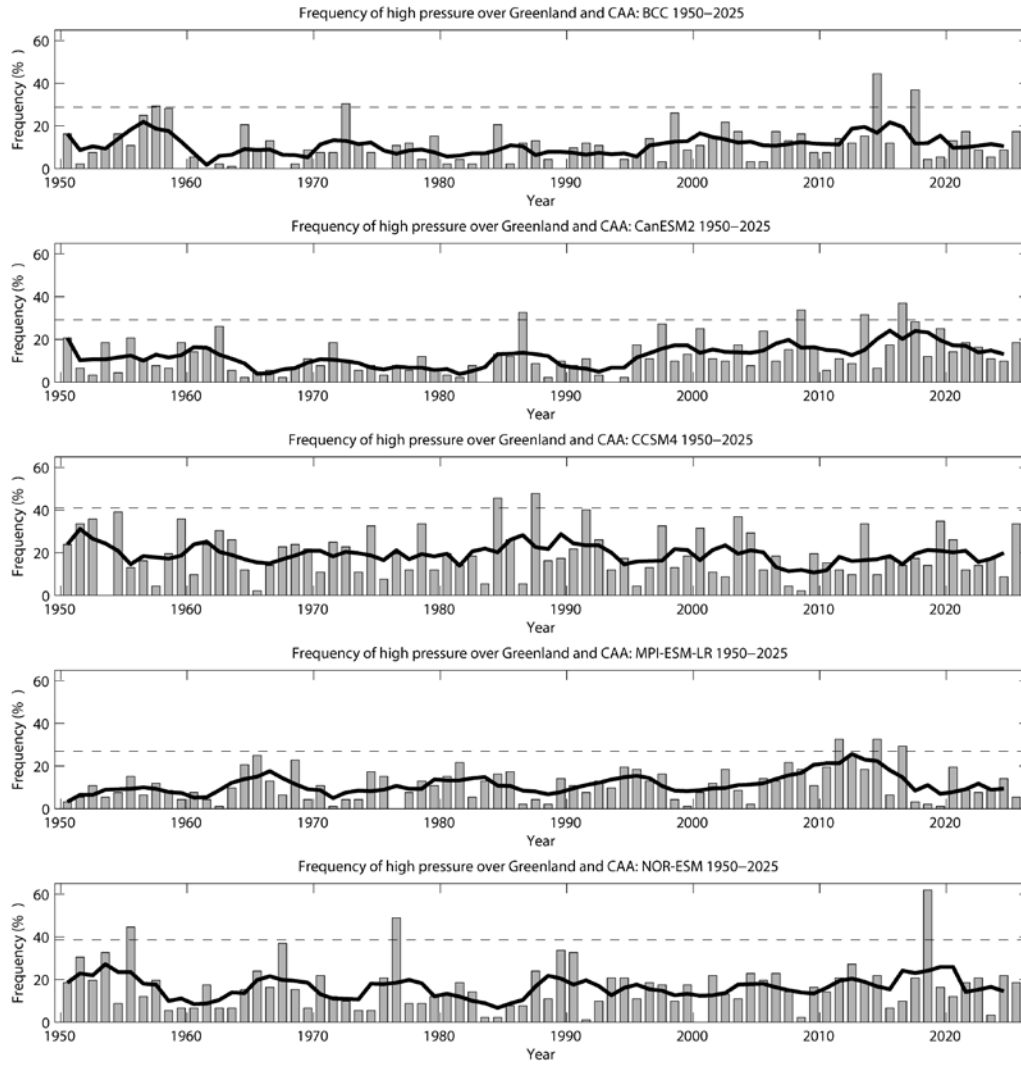
Figure 2-11. Annual summer frequencies of strong positive 500 hPa GPH anomalies identified by the NOI for the five CMIP5 models. The solid line is the 5 year running mean and the horizontal dashed line marks two standard deviations above the climatological mean frequency.
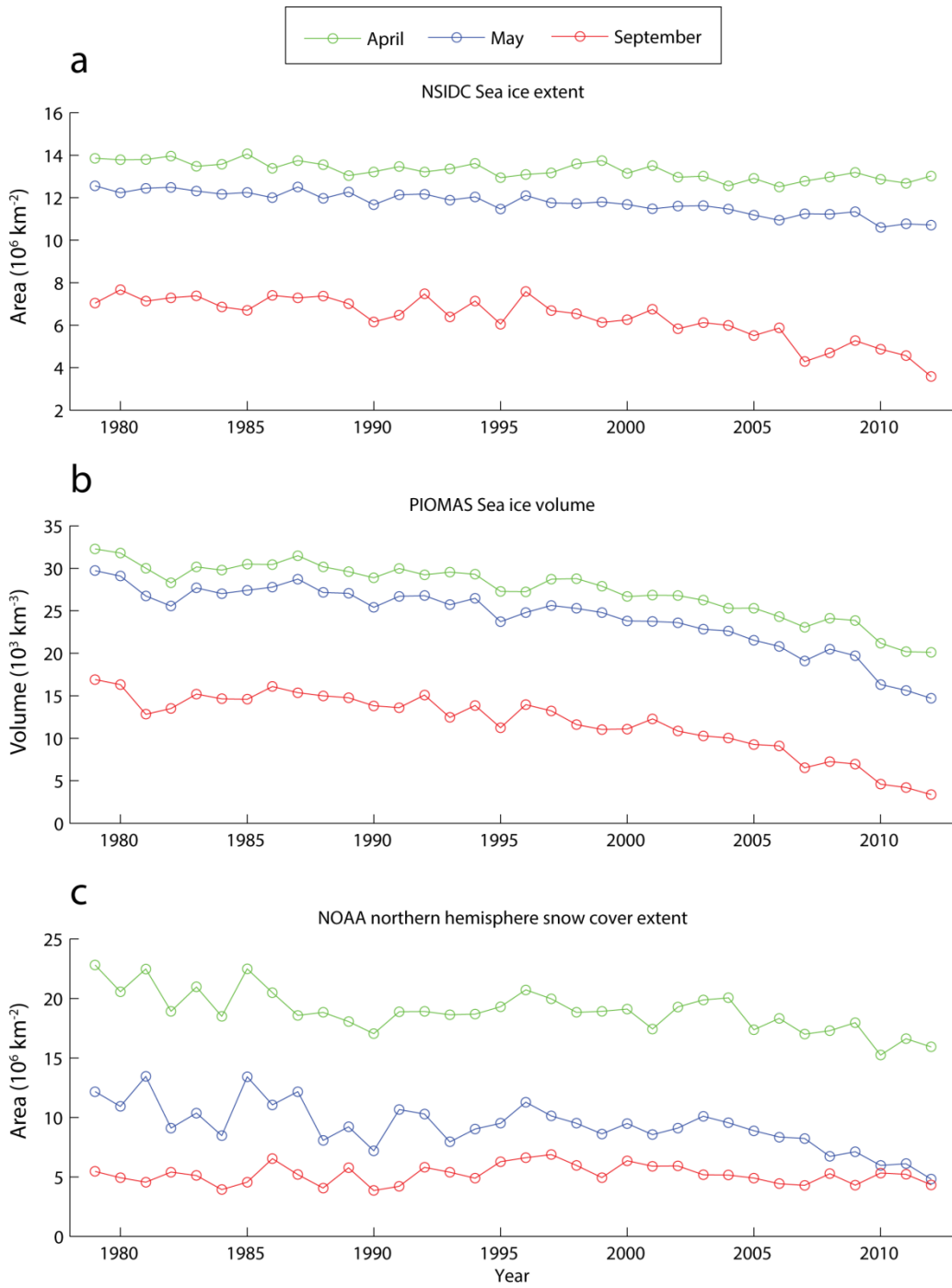
Figure 2-12. April, May and September NSIDC sea ice extent, PIOMAS sea ice volume and Northern Hemisphere spring SCE for 1979-2012.
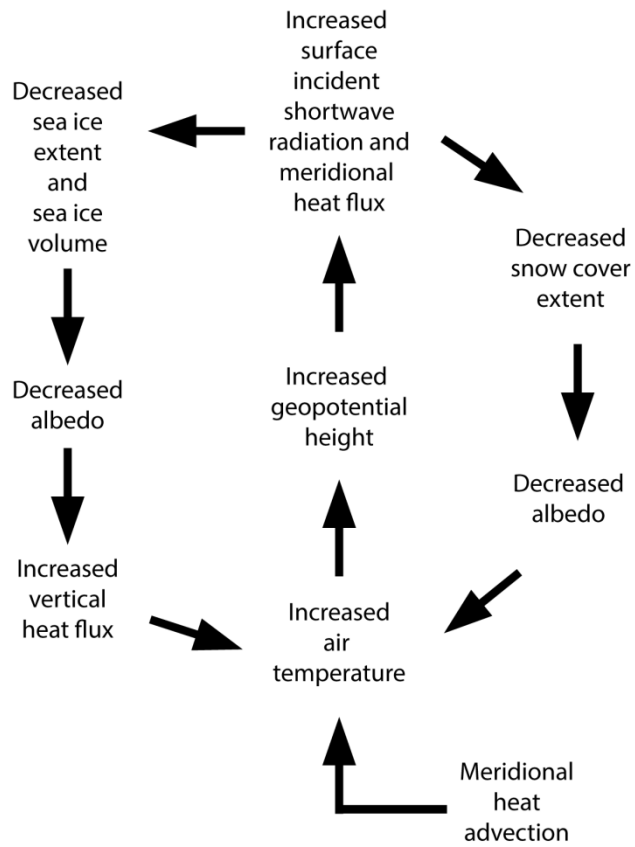
Figure 2-13. Schematic of a multifaceted climate feedback that could potentially drive the rise in frequency of positive GPH anomalies over the CAA and western Greenland between 2007 and 2012.

2.7 References

Alt, B. T. (1978). Synoptic climate controls of mass-balance variations on Devon Island Ice Cap. *Arctic and Alpine Research,* 61-80.

Alt, B. T. (1979). Investigation of summer synoptic climate controls on the mass balance of Meighen Ice Cap. *Atmosphere-Ocean, 17*(3), 181-199.

Alt, B. T. (1987). Developing synoptic analogs for extreme mass balance conditions on Queen Elizabeth Island Ice Caps. *Journal of Applied Meteorology, 26*, 1605-1623.

Belleflamme, A., Fettweis, X., Lang, C., & Erpicum, M. (2012). Current and future atmospheric circulation at 500 hPa over Greenland simulated by the CMIP3 and CMIP5 global models. *Climate Dynamics,* 1-20.

Blüthgen, J., Gerdes, R., & Werner, M. (2012). Atmospheric response to the extreme Arctic sea ice conditions in 2007. *Geophysical Research Letters, 39*(2).

Box, J., Fettweis, X., Stroeve, J., Tedesco, M., Hall, D., & Steffen, K. (2012). Greenland Ice Sheet albedo feedback: Thermodynamics and atmospheric drivers. *The Cryosphere, 6*(4), 821-839.

Braithwaite, R. J. (2005). Mass-balance characteristics of Arctic glaciers. *Annals of Glaciology, 42*(1), 225-229.

Bromwich, D. H., & Wang, S. (2005). Evaluation of the NCEP-NCAR and ECMWF 15- and 40-yr reanalyses using rawinsonde data from two independent arctic field experiments*. *Monthly Weather Review, 133*(12), 3562-3578.

Brown, R. D., & Braaten, R. O. (1998). Spatial and temporal variability of Canadian monthly snow depths, 1946–1995. *Atmosphere-Ocean, 36*(1), 37-54.

Brown, R., Derksen, C., & Wang, L. (2010). A multi‐data set analysis of variability and change in Arctic spring snow cover extent, 1967–2008. *Journal of Geophysical Research: Atmospheres (1984–2012), 115*(D16).

Burgess, D. O. (2012). *Glacier mass balance observations for Meighen Ice Cap, NU, Canada.* Retrieved 03/2013, 2013, from http://pathways.geosemantica.net/ WSHome.aspx?ws=NGP_SECG&locale=en-CA.

Burgess, D. O. (2012). *Glacier mass balance observations for Melville Ice Cap, NWT, Canada. State and evolution of Canada's glaciers, Geological Survey of Canada.* Retrieved 03/2013, 2013, from http://pathways.geosemantica.net/ WSHome.aspx?ws=NGP_SECG&locale=en-CA.

Burgess, D. O., & Koerner, R. M. (2012). *Glacier mass balance observations for Devon Ice Cap NW sector, NU, Canada. State and evolution of Canada's glaciers, Geological Survey of Canada.* Retrieved 03/2013, 2013, from http://pathways. geosemantica.net/ WSHome.aspx?ws=NGP_SECG&locale=en-CA.

Cappelen, J., Laursen, E. V., Jørgensen, P. V., & Kern-Hansen, C. (2011). DMI monthly climate data collection 1768-2010, Denmark, the Faroe Islands and Greenland. *Technical Report 06-09.*

Cassano, J. J., Uotila, P., & Lynch, A. (2006). Changes in synoptic weather patterns in the polar regions in the twentieth and twenty‐first centuries, part 1: Arctic. *International Journal of Climatology, 26*(8), 1027-1049.

Cavalieri, D. J., Gloersen, P., & Campbell, W. J. (1984). Determination of sea ice parameters with the nimbus 7 SMMR. *Journal of Geophysical Research, 89*(D4), 5355-5369.

Chylek, P., Folland, C. K., Lesins, G., Dubey, M. K., & Wang, M. (2009). Arctic air temperature change amplification and the Atlantic Multidecadal Oscillation. *Geophysical Research Letters, 36*(14), L14801.

Cogley, J. G., & Ecclestone, M. A. (2009). Glacier mass balance observations for White Glacier, NU, Canada. A Trent University, Department of Geography contribution to the national glacier-climate observing system, state and evolution of Canada's glaciers, Geological Survey of Canada. Retrieved 03/2013, 2013, from http://pathways.geosemantica.net/ WSHome.aspx?ws=NGP_SECG&locale=en-CA

Derksen, C., & Brown, R. (2012). Spring snow cover extent reductions in the 2008–2012 period exceeding climate model projections. *Geophysical Research Letters, 39*(19).

Durre, I., Vose, R. S., & Wuertz, D. B. (2006). Overview of the integrated global radiosonde archive. *Journal of Climate, 19*(1), 53-68.

Enfield, D. B., Mestas‐Nuñez, A. M., & Trimble, P. J. (2001). The Atlantic Multidecadal Oscillation and its relation to rainfall and river flows in the continental US. *Geophysical Research Letters, 28*(10), 2077-2080.

Fetterer, F., Knowles, K., Meier, W., & Savoie, M. (2002). Sea ice index. *Natl Snow and Ice Data Center, Boulder, CO) Available at Http://nsidc.org/data/g02135.Htm Accessed February, 9*, 2009.

Fettweis, X., Hanna, E., Lang, C., Belleflamme, A., Erpicum, M., & Gallée, H. (2012). Important role of the mid-tropospheric atmospheric circulation in the recent surface melt increase over the Greenland Ice Sheet. *Cryosphere Discussions (the), 6.*

Fettweis, X., Hanna, E., Lang, C., Belleflamme, A., Erpicum, M., & Gallée, H. (2013). Important role of the mid-tropospheric atmospheric circulation in the recent surface melt increase over the Greenland Ice Sheet. *Cryosphere (the), 7.*

Fisher, D., Zheng, J., Burgess, D., Zdanowicz, C., Kinnard, C., Sharp, M., et al. (2012). Recent melt rates of Canadian Arctic ice caps are the highest in four millennia. *Global and Planetary Change, 84*, 3-7.

Foster, J., Cohen, J., Robinson, D., & Estilow, T. (2013). A look at the date of snowmelt and correlations with the Arctic Oscillation. *Annals of Glaciology, 54*, 196-204.

Francis, J. A., & Vavrus, S. J. (2012). Evidence linking arctic amplification to extreme weather in mid‐latitudes. *Geophysical Research Letters, 39*(6).

Frei, A., & Lee, S. (2010). A comparison of optical-band based snow extent products during spring over North America. *Remote Sensing of Environment, 114*(9), 1940-1948.

Gardner, A. S., Moholdt, G., Cogley, J. G., Wouters, B., Arendt, A. A., Wahr, J., et al. (2013). A reconciled estimate of glacier contributions to sea level rise: 2003 to 2009. *Science, 340*(6134), 852-857.

Gardner, A. S., Moholdt, G., Wouters, B., Wolken, G. J., Burgess, D. O., Sharp, M. J., et al. (2011). Sharply increased mass loss from glaciers and ice caps in the Canadian Arctic Archipelago. *Nature, 473*(7347), 357-360.

Gardner, A. S., & Sharp, M. (2007). Influence of the arctic circumpolar vortex on the mass balance of Canadian high Arctic glaciers. *Journal of Climate, 20*(18), 4586-4598.

Gascon, G., Sharp, M., & Bush, A. (2013). Changes in melt season characteristics on Devon Ice Cap, Canada, and their association with the arctic atmospheric circulation. *Annals of Glaciology, 54*, 101-110.

Hanna, E., Fettweis, X., Mernild, S. H., Cappelen, J., Ribergaard, M. H., Shuman, C. A., et al. (2013). Atmospheric and oceanic climate forcing of the exceptional Greenland Ice Sheet surface melt in summer 2012. *International Journal of Climatology*.

Hanna, E., Jones, J. M., Cappelen, J., Mernild, S. H., Wood, L., Steffen, K., et al. (2012). The influence of North Atlantic atmospheric and oceanic forcing effects on 1900–2010 Greenland summer climate and ice melt/runoff. *International Journal of Climatology.*

Helfrich, S. R., McNamara, D., Ramsay, B. H., Baldwin, T., & Kasheta, T. (2007). Enhancements to, and forthcoming developments in the interactive multisensor snow and ice mapping system (IMS). *Hydrological Processes, 21*(12), 1576-1586.

Hewitson, B., & Crane, R. (2002). Self-organizing maps: Applications to synoptic climatology. *Climate Research, 22*(1), 13-26.

Kalnay, E., Kanamitsu, M., Kistler, R., Collins, W., Deaven, D., Gandin, L., et al. (1996). The NCEP/NCAR 40-year reanalysis project. *Bulletin of the American Meteorological Society, 77*(3), 437-471.

Koerner, R. M. (2005). Mass balance of glaciers in the Queen Elizabeth Islands, Nunavut, Canada. *Annals of Glaciology, 42*(1), 417-423.

Kohonen, T. (2001). Self-organizing maps, vol. 30 of springer series in information sciences.

Kohonen, T. (2012). Essentials of the self-organizing map. *Neural Networks, 37*, 52-65.

Lenaerts, J., Angelen, J. H., Broeke, M. R., Gardner, A. S., Wouters, B., & Meijgaard, E. (2013). Irreversible mass loss of Canadian Arctic Archipelago glaciers. *Geophysical Research Letters 40.*

Marzeion, B., Jarosch, A., & Hofer, M. (2012). Past and future sea-level change from the surface mass balance of glaciers. *The Cryosphere Discussions, 60*(4), 3177-3241.

Meinshausen, M., Smith, S. J., Calvin, K., Daniel, J. S., Kainuma, M., Lamarque, J., et al. (2011). The RCP greenhouse gas concentrations and their extensions from 1765 to 2300. *Climatic Change, 109*(1-2), 213-241.

Nghiem, S., Hall, D., Mote, T., Tedesco, M., Albert, M., Keegan, K., et al. (2012). The extreme melt across the Greenland Ice Sheet in 2012. *Geophysical Research Letters, 39*(20)

Oerlemans, J., & Reichert, B. (2000). Relating glacier mass balance to meteorological data by using a seasonal sensitivity characteristic. *Journal of Glaciology, 46*(152), 1-6.

Overland, J. E., Francis, J. A., Hanna, E., & Wang, M. (2012). The recent shift in early summer Arctic atmospheric circulation. *Geophysical Research Letters, 39*(19).

Peixdto, J. P., & Oort, A. H. (1992). Physics of climate. *American Institute of Physics, New York.*

Reusch, D. B. (2010). Nonlinear climatology and paleoclimatology: Capturing patterns of variability and change with self-organizing maps. *Physics and Chemistry of the Earth, Parts A/B/C, 35*(9), 329-340.

Reusch, D. B., Alley, R. B., & Hewitson, B. C. (2005). Relative performance of self-organizing maps and principal component analysis in pattern extraction from s ynthetic climatological data. *Polar Geography, 29*(3), 188-212.

Reusch, D. B., Alley, R. B., & Hewitson, B. C. (2007). North Atlantic climate variability from a self‐organizing map perspective. *Journal of Geophysical Research: Atmospheres (1984–2012), 112*(D2)

Schuenemann, K. C., & Cassano, J. J. (2010). Changes in synoptic weather patterns and Greenland precipitation in the 20th and 21st centuries: 2. analysis of 21st century atmospheric changes using self‐organizing maps. *Journal of Geophysical Research: Atmospheres (1984–2012), 115*(D5).

Schweiger, A., Lindsay, R., Zhang, J., Steele, M., Stern, H., & Kwok, R. (2011). Uncertainty in modeled Arctic sea ice volume. *Journal of Geophysical Research: Oceans (1978–2012), 116*(C8)

Screen, J. A., & Simmonds, I. (2011). Erroneous arctic temperature trends in the ERA-40 reanalysis: A closer look. *Journal of Climate, 24*(10), 2620-2627.

Screen, J. A., & Simmonds, I. (2012). Declining summer snowfall in the Arctic: Causes, impacts and feedbacks. *Climate Dynamics, 38*(11-12), 2243-2256.

Screen, J. A., Simmonds, I., Deser, C., & Tomas, R. (2012). The atmospheric response to three decades of observed Arctic sea ice loss. *Journal of Climate,* (2012)

Serreze, M. C., & Barry, R. G. (2011). Processes and impacts of arctic amplification: A research synthesis. *Global and Planetary Change, 77*(1), 85-96.

Sharp, M., Burgess, D. O., Cogley, J. G., Ecclestone, M., Labine, C., & Wolken, G. J. (2011). Extreme melt on Canada's Arctic ice caps in the 21st century. *Geophysical Research Letters, 38*(11)

Smith, T. M., Reynolds, R. W., Peterson, T. C., & Lawrimore, J. (2008). Improvements to NOAA's historical merged land-ocean surface temperature analysis (1880-2006). *Journal of Climate, 21*(10), 2283-2296.

Steele, M., Ermold, W., & Zhang, J. (2008). Arctic ocean surface warming trends over the past 100 years. *Geophysical Research Letters, 35*(2)

Sterl, A. (2004). On the (in) homogeneity of reanalysis products. *Journal of Climate, 17*(19), 3866-3873.

Stroeve, J. C., Kattsov, V., Barrett, A., Serreze, M., Pavlova, T., Holland, M., et al. (2012). Trends in Arctic sea ice extent from CMIP5, CMIP3 and observations. *Geophysical Research Letters, 39*(16).

Taylor, K. E., Stouffer, R. J., & Meehl, G. A. (2012). An overview of CMIP5 and the experiment design. *Bulletin of the American Meteorological Society, 93*(4), 485-498.

Tedesco, M., Fettweis, X., Mote, T., Wahr, J., Alexander, P., Box, J., et al. (2013). Evidence and analysis of 2012 Greenland records from spaceborne observations, a regional climate model and reanalysis data. *Cryosphere Discussions (the), 6.*

Walsh, J. E., & Chapman, W. L. (1990). Short-term climatic variability of the arctic. *Journal of Climate, 3*(2), 237-250.

Wang, M., & Overland, J. E. (2012). A sea ice free summer Arctic within 30 years: An update from CMIP5 models. *Geophysical Research Letters, 39*(18)

Zdanowicz, C., Smetny‐Sowa, A., Fisher, D., Schaffer, N., Copland, L., Eley, J., et al. (2012). Summer melt rates on Penny Ice Cap, Baffin Island: Past and recent trends and implications for regional climate. *Journal of Geophysical Research: Earth Surface (2003–2012), 117*(F2)

Zhang, J., & Rothrock, D. (2003). Modeling global sea ice with a thickness and enthalpy distribution model in generalized curvilinear coordinates. *Monthly Weather Review, 131*(5), 845-861.

Chapter 3

3.1 Introduction

The climate of the Canadian Arctic is characterized by low inter-annual variability in precipitation, and by high inter-annual variability in summer air temperature. Thus, changes in the annual mass balance of ice caps and glaciers in the region are strongly linked to variations in summer climate and snow/ice melt (Oerlemans and Reichert, 2000; Koerner, 2005). NCEP R1 reanalysis data (dating back to 1948) indicate that the highest regional mean summer air temperatures at 700 hPa geopotential height in the 64 year record (1948-2012) occurred between 2000 and 2012, and especially after 2005 (Sharp et al., 2011). Summer melt records derived from variations in the abundance of melt layers in ice cores from four ice caps in the Canadian Arctic show that recent melt rates are the highest in the last 4,000 years, and approach those seen in the Holocene thermal maximum, approximately 9,000 years ago (Fisher et al., 2012; Zdanowicz et al., 2012). Around 147,000 km^2 of the 540,000 km^2 of ice caps and glaciers outside Greenland and Antarctica are found in the Canadian Arctic. As a result of the post-2005 summer warming, this region has emerged as one of the most important regional non-ice-sheet sources of global sea level rise (Gardner et al., 2011).

From the 1960s until the early 21st century, firn compaction on ice caps in Arctic Canada occurred under conditions of relatively consistent mean annual air temperatures (MAAT) and annual snow accumulation rates (Koerner, 1977; Gardner and Sharp, 2007; Colgan and Sharp, 2008; Hörhold et al., 2011). As a result, firn density-depth profiles were likely relatively constant over time, as assumed in Sorge's Law (Bader, 1953). However, observations on the Penny Ice Cap, Baffin Island, show significant recent increases in firn density, ice fraction, and 10-15 m firn temperatures that are consistent with observations of increasing air temperature and melt rates since the mid-1990s (Zdanowicz et al., 2012). Here we explore whether similar changes in the firn profile have occurred on Devon Ice Cap, Nunavut, located further north in the Canadian Arctic,

59

and evaluate the extent to which they may influence the interpretation of altimetrically-determined rates of surface height change on these ice caps in terms of changes in ice cap mass balance.

We present the results of an ice coring campaign conducted in spring 2012 that was designed to measure profiles of firn density, ice content, and temperature in the accumulation zone of the Devon Ice Cap. Twenty ice cores were recovered from sites in the summit region of the ice cap (1800-1900 m a.s.l.) and along an 18-km long section of the "CryoSat line". This transect extends south from the summit region of the ice cap and spans elevations from 1400-1800 m a.s.l. These cores are coincident in location with 34 firn cores drilled between 2004 and 2011, while the cores recovered at 1800 m a.s.l. are comparable in location with deep ice cores drilled in 1971 and 1972 (Koerner, 1977; Paterson and Clarke, 1978). Using this spatially and temporally rich data set, we describe the physical and thermal impacts of recent summer warming and associated melting on the upper 15 m of the firn layer of the Devon Ice Cap.

3.2 Study Site

The ~14,000 km^2 Devon Ice Cap is located on the eastern end of Devon Island, in Canada's Queen Elizabeth Islands (Figure 3-1), and is one of the larger ice masses in the Canadian Arctic. The ice cap and its outlet glaciers extend from sea level to 1920 m a.s.l. Historically, the accumulation zone included a quasi-dry-snow zone (where surface melt occurred in some, but not all, years), a percolation zone, a wet-snow zone, and a superimposed ice zone (Koerner, 1977).

The Devon Ice Cap has a multi-decadal record of in-situ observations, starting in 1961. These include annual surface mass balance measurements, firn/ice core records, air temperature measurements from automatic weather stations (AWS) and HOBO air temperature sensors, and repeated kinematic GPS and GPR surveys (Boon et al.,

2010). In 2004, 3 AWS and 15 HOBO air temperature sensors were installed along the entire CryoSat line, which spans an elevation range from 400-1800 m a.s.l. Along this line, mass balance stakes were placed approximately every kilometer, and HOBO air temperature sensors approximately every three kilometers. Within the accumulation zone, AWS were located near the ice cap summit, and at Sites 1 and 2 (Figure 3-1).

The summit AWS is located on the south flank of the summit ridge, at 1900 m a.s.l. Site 1 is on the southwestern side of the summit plateau, and marks the upper limit of the CryoSat line (1800 m a.s.l.). Site 2 is located 18 km down the transect from Site 1, at 1400 m a.s.l. HOBO air temperature sensors were mounted on mass balance stakes located at 4.7 km, 9.1 km, and 13.7 km from Site 1.

3.3 Data Sets and Methods

3.3.1 Firn Cores

We analysed 54 firn cores that were recovered from 20 distinct locations on the ice cap in either April or May, between 2004 and 2012 (Figure 3-1). Forty of the 54 cores extended to depths of 2.5-5 m, and the remaining 14 cores to depths of 15-21 m. Cores were recovered using a Kovacs MK II corer with an internal barrel diameter of 9 cm. The stratigraphy and density profiles from these firn cores provide information about environmental conditions on the ice cap in the years prior to their recovery.

While a significant number of ice cores from the Devon Ice Cap are available for analysis, the data set has some limitations. Ice cores recovered prior to 2012 were collected as components of past experiments, and not for the explicit purpose of updating the melt record. For example, only the top 3 m of the 20-m ice cores recovered in 2004 were documented. In 2006, ice cores with depths ranging from 2.5 m to 3.2 m were recovered at most of the mass balance poles along the CryoSat line. The lengths

of these cores limit the depth range over which firn profile changes along the CryoSat line can be investigated.

To derive firn density profiles, the mass and length of each core section were measured in the field. Core section lengths (generally 20 cm to 40 cm) were determined by natural breaks created during the coring process. Observations of firn core stratigraphy were made using two methods. Prior to 2012, firn stratigraphy was documented by direct visual logging of the core, either in the field or after return to a cold laboratory. Firn types (e.g., dry firn, wetted firn, soaked firn) and ice layers were differentiated on the basis of firn density and air bubble content/size. Firn cores recovered in 2012 were documented with a Fuji FinePix S9000 digital camera, modified to capture visible and infrared (IR) wavelengths between 330 nm and 1200 nm. The full length of each core was laid out on the ice cap surface next to a 30-m survey tape, and shaded with a neutral grey backdrop. One-meter sections of firn core were photographed twice, first with a filter blocking wavelengths shorter than 850 nm, and then with a filter blocking wavelengths shorter than 1000 nm.

On the ice cap, IR photography was considerably faster than manually logging cores, allowing for a larger number of cores to be sampled during the short field season. In the IR photographs, ice layers show up as dark grey layers, while firn layers remain white with observable texture patterns that allow for the distinction of different ice crystal types and sizes. Differentiating ice and firn in the photographs is straightforward, but there is more subjectivity in classifying the different types of firn. Firn stratigraphy was therefore plotted using two classes: firn and ice. This simplification was made in order to reduce the impact of classification biases resulting from different observers, and the subjective description of firn types and characteristics. Layers plotted as firn in this paper were originally described as either dry firn, depth hoar, wetted firn, soaked firn, or icy firn. While this simple classification limits detailed comparisons of firn stratigraphies, it

greatly improves our confidence that we are observing true physical changes rather than observer-related changes in firn classification.

3.3.2 Ice Fraction

The ice fraction is a simple metric to describe the firn profile. Spatial and temporal changes in the ice fraction reflect variations in both the amount of melt occurring at the surface and the extent to which meltwater infiltrating the firn refreezes within the firn body. To form ice layers within the firn column and/or the winter snowpack, infiltrating meltwater must come into contact with snow and/or firn at sub-freezing temperatures. Firn temperatures measured at 1 m depth intervals in the upper 1-8 m of boreholes at Sites 1 and 2 in 2012 ranged between -16°C and -22°C. These temperatures are sufficiently low to allow significant internal refreezing of surface-derived meltwater following the onset of surface melt in late spring and early summer.

The simplified ice fraction of each core section was calculated, following Koerner (1977) and Fisher et al. (2012).

$$Ice\ Fraction = \frac{\sum Ti}{L} \times 100$$

Expressed as a percentage, the simplified ice fraction equals the sum of the thickness of the ice layers (in meters of water equivalent (m w.e.)) (T_i), divided by the total length of the ice core in m w.e. (L), multiplied by 100. Since only bulk densities were measured in the field, ice layers were assigned a density of 875 kg m^{-3}, the mean density of a sample of core sections containing 100% ice. The ice fraction was calculated for the entire length of each core using the stratigraphic record to identify ice layers and the density profile to calculate the total length (in m w.e.) of the firn column. No correction was made for flow-induced layer thinning, since the top 18.5 m of firn is assumed to have undergone negligible flow-induced deformation (Pohjola et al., 2002).

3.3.3 Density Changes

Empirical firn depth-density relationships provide a simple and effective method for calculating the firn density profile in Polar regions. Such empirical relationships are typically based on *Sorge's Law* (a steady state firn depth-density profile), which applies where accumulation rates and summer melt conditions are constant over time (Bader, 1953). To assess the continued validity of these empirical depth-density relationships, 15 m firn density profiles for the Colgan B, C and E sites were compared to the theoretical firn density profile calculated using the depth-density equation found in Cuffey and Paterson (2010, p 19).

$$\rho(z) = \rho_i - [\rho_i - \rho_s]\exp(-\frac{z}{z_\rho})$$

Here, density at a prescribed depth ($\rho(z)$) is a function of the density of ice (ρ_i), the density of the spring snowpack (ρ_s), the depth (z) and a site constant (z_ρ). For the Devon Ice Cap, the mean densities of ice (875 kg m^{-3}) and snow (320 kg m^{-3}) were calculated from ice cores and snow pits. The site constant was calculated from the 2004/2005 firn profiles using a least squares method to determine the best fit. For the three core sites Colgan B, C and E, the best fitting site constants were calculated to be 19, 11 and 10 respectively.

3.3.4 Thickness Changes

To assess the potential impact of changes in the firn densification rate on the ice cap surface elevation, changes in the thickness of a surface layer containing 1.25 m water equivalent (w.e.) were estimated from repeat measurements of density profiles at individual locations. The value of 1.25 m w.e. equates to the w.e. of the minimum available core length in 2006. Previous work using chemical analysis of ice cores and the depth of the 1963 "bomb layer" (a horizon line resulting from the atmospheric fallout of thermonuclear bomb testing and measured by down borehole ^{137}Cs gamma spectrometry) found net accumulation rates in the study area to be ~0.23 m w.e. per

year (Mair et al, 2005; Colgan and Sharp, 2008). Given this accumulation rate, 1.25 m w.e. of firn would represent 5.4 years of net accumulation. This method of estimating near surface firn thickness changes does not account for densification below a depth of 1.25 m w.e., and assumes that winter accumulation rates are constant from year to year, an assumption that is consistent with annual (2004-2012) measurements of spring snowpack depths made at multiple locations along the CryoSat line between 1350 m a.s.l. and 1850 m a.s.l. These measurements show a trend of only ~+0.01 m a^{-1} over the eight year period.

To provide a context for assessing the significance of the magnitude of the computed changes in firn thickness since 2004, surface height changes for the period 2004-2012 were calculated by comparing repeat airborne laser altimeter profiles measured along the CryoSat line in the springs of 2004 and 2012. On May 2, 2004, an elevation profile was measured with a Riegl LMSQ-280 laser scanner (www.riegl.com) mounted on the Alfred Wegener Institute's Dornier 228 aircraft. On May 4, 2012, the elevation profile was re-measured as part of Operation IceBridge using NASA's Airborne Topographic Mapper (ATM) onboard a P-3B aircraft (Krabill, 2012). The vertical accuracies of both datasets are estimated to be +/- 10cm. The net change in surface height was calculated at 10 m intervals along the CryoSat line by differencing the elevations of points measured in 2004 and 2012 that were located within three meters of each other. To assess the relationship between changes in local firn properties and rates of surface height change, annual surface height change measurements along the CryoSat line were aggregated into five 100 m elevation bins covering the altitude range from 1350 to 1850 m a.s.l.

3.3.5 Firn Temperatures

Firn temperature profiles were measured in 7 of the 15 m boreholes drilled in 2012 using 10 kOhm NTC thermistors (accuracy ±0.1°C). The thermistor string design and

installation followed Humphrey et al. (2012). Assembled thermistor strings were lab-calibrated using an ice-bath to verify accuracy. Following extraction of a firn core, a thermistor string was weighted and suspended in the borehole to ensure that the wire was taut and reached a depth of 15 m. Dry snow and core shavings were used to backfill the hole. To determine the duration of the thermal disturbance caused by drilling and backfilling of the borehole, a data logger (Campbell Scientific CR10X) was attached to the Site 1 thermistors immediately after burial. These thermistors were read using three-wire half bridges, and readings stabilized within three hours and remained constant for the following 16 days. This timescale for stabilization of firn temperatures is consistent with the observations of Humphrey et al. (2012) and indicates (i) that thermal energy added or removed as a result of drilling and backfilling had dissipated into the surrounding firn by the time that profile measurements were made, and (ii) that the observed temperatures reflect the local firn temperature. All thermistors were left to stabilize for a minimum of 24 hours before measurements were made using a Uni-Trend UT33C multimeter. Thermistors were measured on three or four days, and readings were averaged to minimize the effect of measurement error. The mean standard deviation of firn temperature readings was 0.58°C and the range of standard deviations was from 0.23°C to 1.11°C.

The 2004 firn temperature at Site 1 was measured during the installation of the CryoSat line. This measurement was taken by suspending a HOBO temperature sensor 10 m down the borehole and allowing it to record for 24 hours. The method used to record the 2012 temperatures was similar to that used in 1971 and 1972, as detailed in Paterson and Clarke (1978). It incorporated redundancy and measurement verification by installing pairs of thermistors spaced 2 to 5 m apart down the length of the borehole.

 Mean annual air temperatures (MAAT) were calculated using data from the AWSs at the summit (established in 1997) and Site 2 (established in 2004), and from the HOBO

air temperature sensors at HB 4-7, HB 9-1, and HB 13-7 (all established in 2004). Due to equipment malfunctions and data loss, only one continuous year of temperature measurements was recorded at the Site 1 AWS, so these data were excluded from the analysis. At the summit and Site 2 AWS, Campbell Scientific 107B and 107F thermistors (accuracy ±0.4°C) were installed in Campbell Scientific Gill radiation shields 1–2 m above the spring snow surface and measured temperatures every minute and recorded hourly averages. At HB 4-7, HB 9-1, and HB 13-7, air temperatures were recorded with HOBO Pro Series and HOBO Pro Series v2 loggers (accuracy ±0.7°C) installed in Onset RS1 radiation shields, positioned 1–1.5 m above the spring snow surface. The range of temperature sensor heights is primarily a result of the seasonal cycle of accumulation, ablation and firn compaction. The sensor heights are typically at a minimum in the spring following winter accumulation, and at a maximum in the fall following summer ablation and firn compaction. Measurements from a Campbell Scientific SR50 sonic ranger located on the Site 2 AWS show that sensor height varies by ~0.5 m annually. As a result of equipment failure and the extreme environmental conditions on the ice cap, data gaps are present in all the temperature records. Only complete years of records were used to calculate the MAAT. The MAAT values for the summit, HB 4-7, HB 9-1, HB 13-7, and Site 2 were calculated using 9, 4, 5, 2, and 6 years of data, respectively. The start of a year is defined by the spring date (mid-April to mid-May) on which the weather station was serviced and data were downloaded. The service date, rather than a fixed date, was chosen to define the beginning of a year because it allowed for the maximum number of years to be used in the MAAT calculations.

For comparison, and to extend the air temperature records, the 700 hPa MAAT over the ice cap was calculated from the National Centers for Environmental Prediction and National Center for Atmospheric Research (NCEP) Reanalysis 1 project (Kalnay et al., 1996). Sharp et al. (2011) demonstrated that mean summer surface air temperatures in

the accumulation zones of the Devon and Agassiz Ice Caps were well correlated with the 700 hPa NCEP R1 mean summer air temperatures over the respective ice cap.

3.4 Results and Discussion

3.4.1 Firn Stratigraphy

A recent increase in the number and thickness of ice layers in the top 3 meters of firn is apparent at all sites. This is especially evident at the Colgan B, C, and E core sites (Figure 3-2), for which we have 15 m observations for 2004/2005 and 2012. The shallower cores recovered in 2012 along the CryoSat line (Figure 3-3) also show an increase in ice content relative to the cores retrieved in 2004/2006 and the spatial pattern of change clearly illustrates that the upper limit of firn containing ice layers accumulated over multiple years has shifted to higher elevations since 2004/2005.

To quantify the change in stratigraphy between 2004/2005 and 2012, we calculated the simplified ice fraction for each year for the Colgan B, C and E core sites (Table 3-1). At Colgan B and E, the ice fraction increased at each site from 31.1% and 51.4% respectively in 2004/2005 to 45.0% and 58.5% in 2012. The ice fractions for the Colgan C core site can be compared with that reported for the deep cores drilled in 1971 and 1972, as the sites are separated horizontally by ~7 km, but by only ~15 m in elevation (Koerner, 1977). The ice fraction in the top 20 m of the 1971/1972 cores was ~15%, which is similar to that observed in 2004 (16.4%), but by 2012 it had increased to 30.3%. Linear regressions of the NCEP-NCAR 700 hPa air temperatures over the summit of Devon Ice Cap against time for the period 2005-2012 show the mean December, January and February temperature has decreased by 0.19°C while the mean June, July and August air temperature has increased by 0.16°C. The resulting 0.35°C increase in summer-winter temperature contrast may be a contributing factor to the observed increase in ice content of the firn (c.f. Pfeffer and Humphrey, 1998).

Comparing the 2012 stratigraphic plots for the three Colgan sites with those from 2004/2005, it is evident that there has been a notable decrease in the number of very thin ice lenses. We believe this is a result of using the photographic method to record firn stratigraphy in the field in 2012. While the pictures were taken at the highest quality setting and stored in a RAW file format to avoid detail loss due to file compression, some millimeter-scale ice lenses that were visible in the field are not visible in the images. There are two possible explanations for the apparent disappearance of millimeter- scale ice layers in the 2012 images. The first is that an experienced human observer may be able to record a more detailed stratigraphy when viewing a firn core directly than when viewing IR images of it. Unfortunately, we do not have in-situ stratigraphic logs from 2012 to verify this hypothesis. The second is that increased melt rates since 2004/2005 have resulted in millimeter-scale ice layers being replaced by the thicker ice layers that are visible in 2012. The disappearance of millimeter-scale ice layers has ramifications for the calculation of ice fraction presented above. The values for 2012 are likely underestimated relative to the values from 2004/2005 but, despite this, the ice fraction at all three Colgan sites increased between 2004/2005 and 2012.

Shallow cores recovered along the CryoSat line reveal changes in the distribution of snow and firn facies within the accumulation zone since 2004 (Figure 3-3). At that time, Site 1 was located near the boundary between the quasi-dry-snow zone and the percolation zone, and Site 2 was located in the wet snow zone (Bell et al., 2008). These facies are visible in the core stratigraphy from 2004, where, Site 1 has discrete sub-decimeter thick ice layers and Site 2 has meter thick ice layers separated by firn layers. Surveys made in the 1960s located the superimposed ice zone between 1100 m a.s.l. and 1300 m a.s.l. on the south side of the Devon Ice Cap (Koerner, 1970). By 2012, cores composed almost entirely of ice were retrieved from locations between Site 2 (1400 m a.s.l.) and MB 11-5 (1550 m a.s.l.), indicating that the lower limit of the wetted snow zone and the upper limit of the superimposed ice zone had increased in elevation

by ~150 m since 2004. Increased surface melt since 2005 has resulted in large volumes of meltwater being stored in the upper firn column as infiltration ice. After several consecutive years of substantial internal accumulation, the infiltration ice layer appears to have become impermeable to meltwater percolation. As a result, meltwater from subsequent years refreezes on top of the previous summer's ice layer and the superimposed ice zone has effectively extended up-glacier over the top of residual firn that is now hydrologically isolated from the glacier surface.

The effects of climatic change can also be seen in the 15 m firn profiles measured in 2012 at HB 9-1, HB 13-7, and Site 2 along the CryoSat line. In Figure 3-4, we compare the stratigraphy of the bottom third of each core with that of the top third of the core to assess decadal-scale changes. The 1963 "bomb layer" provides a scale for time as a function of depth in the recovered cores. It was found at 10.2-10.6 m depth in three cores drilled south of the summit between 1367 m a.s.l. and 1504 m a.s.l. in 2000, and at 11.5m in a core drilled at 1525 m a.s.l. in 2005 (Mair et al., 2005; Colgan and Sharp, 2008). The depth of the bomb layer was not measured in 2012, but based on its depth in 2000 and 2005, we believe that the 15 m cores recovered in 2012 represent at least 50 years of net accumulation. There are clear changes in ice fraction and firn density between the lower and upper halves of the firn cores from all three sites. At Site 2 and HB 13-7, near-continuous ice is visible down to 6.5 m and 5.5 m respectively. At HB 9-1, the impact of higher melt rates is evident from the higher ice fraction in the top 5.5 m of the core, although the core from this site is not yet composed entirely of ice. The increase in near-surface firn density over time is also evident at higher elevations. The impermeability of the infiltration/superimposed ice layer has ramifications for calculations of the meltwater storage potential of the underlying firn, and for the likelihood of supraglacial runoff from this part of the accumulation area of the ice cap, as it appears unlikely that pore space in the underlying firn will ever be homogenously filled with infiltration ice.

3.4.2 Firn Density

Given the recent increase in the ice content of cores from all sites, an increase over time in the density of the top 2.5-3 m of firn was anticipated. To assess the magnitude of changes in firn density at the three Colgan core sites, density profiles from 2004/2005 are plotted alongside those from 2012 (Figure 3-5). Profiles from 2004/2005 show a general trend of increasing density with depth, but this trend is not evident in the 2012 profiles, in which densities increase upwards in the top 3–4 m. This change is clearly illustrated by plots of the difference between the 2004/2005 and 2012 density profiles. In the density difference plots, there are a number of layers in the top 3 meters for which the density change exceeds two standard deviations of the mean density in the bottom 10 meters of the core. This demonstrates that the density changes observed in the top three meters of the firn layer are well above what is attributable to historically normal climatic variability. Firn density increases significantly upwards in the top 3 meters of the Colgan B and C cores. At Colgan E, there is more variability in the pattern of firn density changes in the top 3 meters, but the increases are larger than the decreases. At depths greater than 3 meters, the changes in firn density tend to be slightly negative. A peak in the magnitude of density decrease is evident between 3 and 4 m depth at all sites. One possible explanation for this is that a thick ice lens known to have formed in 2005 (the first year of extreme melt) created an impermeable barrier for both meltwater percolation and the transport of sublimated water vapor, causing the formation of a well developed depth hoar layer below the ice layer. As a result, in subsequent years, meltwater that would typically have percolated downwards and refrozen to increase the density of deeper firn layers instead pooled and refroze on top of the 2005 ice layer, increasing the density higher in the firn profile.

Empirical relationships provide a method for calculating the firn density profile in the absence of in situ observations. Since these relationships are based on the assumption

of steady state climatic conditions, it is important to assess their validity under changing climatic conditions. Figure 3-5 compares the measured 15 m firn density profiles for the Colgan B, C and E sites with the empirically derived firn density profile (thick grey line). Here, it is apparent that the density of the top 2.5-3 m of firn has increased to well above the expected values. For the full length of all three cores, the mean percentage difference between the empirically-estimated and measured densities increased from 16.1% to 33.8% over the period from 2004/2005 to 2012. For the top 4 m, the mean difference increased from 33.1% to 67.3% over the same period. This clearly suggests that, during periods of climate warming, the use of Sorge's Law to estimate the density of material added to, or removed from, the surface of a firn layer over time is problematic.

Based on the density profiles from the Colgan sites, the top 3 meters of firn appear to have been most strongly affected by increasing meltwater penetration and refreezing, resulting in density increases. To expand the scope of our analysis of density changes, we calculated the average density of a 2.5 m thick column of firn (measured downwards from the firn surface) for each of the shallow core sites along the CryoSat line that were sampled in 2004/2006 and 2012, and for the three Colgan sites that were sampled in 2004/2005 and 2012 (Table 3-2). All sites show a higher average density in the top 2.5 m of the profile at the time of the most recent coring than at the time of first coring. The average density increase ranged between 13.0% and 80.3%, and was generally larger at elevations below MB 11-5 (~1490 m a.s.l.) than above that location. Above MB11-5, the mean change in average density was 25.7 ± 8.5%. Below MB 11-5, it was 44.1 ± 16.7%.

Assuming a constant snow accumulation rate, the observed density increase in the upper 3m of the firn can be interpreted as being largely a response to increased surface melt and internal refreezing. It also provides an indication of the ability of firn layers to

absorb meltwater. Since increased ice content indicates a reduction in available pore volume, it is very likely that the thickness of the firn layer that contains a given mass of water has decreased since the mid 2000's. Again, assuming constant accumulation rates, this would have resulted in a lowering of the ice cap surface. This effect should be taken into account when estimating the mass change associated with altimetrically-determined lowering of the ice cap surface.

3.4.3 Firn Thickness Changes

Firn thicknesses associated with the upper 1.25 m w.e of each core in 2004-6 and 2012 are presented in Table 3-3. The rate of decrease in the thickness of this layer over time ranges from 0.021 m a^{-1} to 0.168 m a^{-1}. The largest rates were found in the region between MB 10-3 and MB 15-9 (1430-1575 m a.s.l.), where there has been significant accumulation of infiltration ice within the firn since 2004.

To determine whether the thinning of the uppermost part of the firn column that has been affected by more rapid densification could have caused changes in the elevation of the ice cap surface, we compared the computed thinning rates with available measurements of surface height change in the study region. Repeat airborne laser altimetry surveys conducted in 1995 and 2000 found that the summit region of the Devon Ice Cap was thickening at a rate of 0.20 m a^{-1} (Abdalati, et al., 2004). Using mean annual net accumulation rates and measurements of ice discharge from the summit region through a series of flux gates, Colgan et al. (2008) calculated the mean rate of ice cap thickness change between 1963 and 2003 to be 0.01 ±0.12 m w.e. a^{-1}. Repeat airborne laser altimetry measurements made between 2004 and 2012 suggest that the 1995-2000 trend of increasing surface elevation in the summit region appears now to have been reversed (Table 3-4). Mean rates of surface elevation change over the 2004-2012 period ranged from -0.077 m a^{-1} in the 1750-1850 m elevation bin to -0.252 m a^{-1} in the 1350-1450 m bin. These changes are attributable to some

combination of variability in the winter snowpack thickness and density, changes in the rate of firn densification over the full depth of the firn profile, changes in the rate of ice flow, and (especially at lower elevations) changes in meltwater runoff.

Observed rates of change in the thickness of the end-of-winter snowpack have been relatively constant ($+0.01$ m a^{-1}), and are both small and of opposite sign to the observed rates of surface elevation change. The period of observation (2004-2012) is likely too short for significant changes in the rate of ice flow to have occurred as ice flow in the high elevation region of the Devon Ice Cap is governed by rates of ice deformation, rather than basal sliding or bed deformation (Burgess et al., 2005). Although we lack the data required to estimate the change in the rate of firn densification for the full firn profile, it is clear that the estimated rates of change in the thickness of the upper 1.25 m w.e. of the firn layer alone are large relative to the magnitude of observed surface elevation changes. This is particularly apparent in the upper two elevation bins (1650-1750 m a.s.l. and 1750-1850 m a.s.l.), where the increase in firn density can account for 77% and 90% of the observed surface height change respectively. This strongly suggests that more rapid firn densification is contributing significantly to the recently observed decrease in surface elevation of the summit region of the Devon Ice Cap. Since this acceleration of firn densification is linked to increased storage of meltwater as ice layers within the firn, it is probable that the latent heat released during refreezing will have raised the firn temperature at 10-15 m depth (the level at which the annual cycle of variations in air temperature no longer affects the firn temperature) relative to both historic measurements and the mean annual air temperature.

3.4.4 Firn Temperatures

The difference between firn temperatures at 10-15 m depth and local mean annual air temperatures provides an indication of the magnitude of meltwater penetration and

refreezing. In the absence of internal refreezing, the 10 to 15 m firn temperature approximates the mean annual air temperature (Paterson and Clarke, 1978; Humphrey, Harper and Pfeffer, 2012). When internal refreezing occurs within the firn, however, latent heat is released and can warm the surrounding firn. Firn temperature profiles were measured in boreholes drilled at sites ranging in elevation from 1400-1900 m a.s.l. The MAAT at Site 2 is -17.7°C while the 10 m and 15 m firn temperatures are -14.6°C and -14.3°C, respectively (a difference of +3.1-3.4°C). At the summit, where the MAAT is -20.5°C, the 10 m and 15 m firn temperatures are -18.9°C and -18.5°C, respectively (a difference of only +1.6-2.0°C) (Figure 3-6A). This suggests that, as expected, the magnitude of firn warming due to latent heat release during refreezing decreases with increasing elevation.

The longest time series of firn temperatures is available for the summit plateau, a very broad ridge to the west of the ice cap summit with elevations ranging from 1800-1825 m a.s.l. The 1971 and 1972 ice cores were drilled ~8 km northeast of Site 1, at an elevation of 1825 m a.s.l. Paterson et al. (1977) reported the MAAT for these core sites in 1971 and 1972 as -23°C. The Summit AWS, which is ~100 m above these core sites, had a MAAT for the period 1997-2008 of -20.5°C, suggesting warming of perhaps 2.5°C since the early 1970s. To put these observations into perspective, the 700 hPa MAATs from the NCEP R1 Reanalysis are shown in Figure 3-7. Although there is a large degree of variability, linear regression suggests the MAAT increased by ~1.5°C since 1990 and ~1.8°C since 1970.

Figure 3-6B shows the observed firn temperatures on the Summit Plateau in 1971/1972, 2004, and 2012. In 1971/1972, firn temperatures at 10 m and 15 m were -23.2°C and -23.1°C, respectively. In 2004, the 10 m firn temperature at Site 1 (located on the southwestern edge of the Summit plateau) was -21.3°C, but by 2012, the firn temperature at that location had risen to -17.5°C at 10 m and -17.4°C at 15 m. Thus,

while the MAAT has increased by ~ 1.8°C since 1970, the 10 m and 15 m firn temperatures have increased by ~ 5.7°C. Between 2004 and 2011, the 10 m firn temperature at Site 1 rose by 3.8°C. Based on a linear regression from 2004-2011, the MAAT rose by 1.0°C, leaving 2.8°C of warming that could be attributed to warming by latent heat released by freezing meltwater.

The potential rise in firn temperature at 15 m that could be attributed to latent heat released by refreezing of meltwater can be estimated from the gain in mass of the top 2.84 m of the firn (depth to the bottom of the major ice layers) since 2004. Although the source of latent heat is assumed to be located at the top of the firn column (because ice buildup in the upper part of the firn column limits vertical percolation of meltwater), it is assumed to raise the firn temperature uniformly across the upper 15 m of the profile. At Site 1, the latent heat released between 2004 and 2012 would have been sufficient to warm the upper 15 m of firn by 2.5°C. The total warming due to air temperature changes and latent heat released during refreezing is therefore ~ 3.5°C, which is comparable to the measured warming (3.8°C).

These observations are consistent with recent observations from west Greenland and the Penny Ice Cap, Baffin Island (Humphrey, Harper and Pfeffer, 2012; Zdanowicz et al., 2012). In western Greenland, 10 m firn temperature rose by 0.45-2.6°C per year between 2007 and 2009 (Humphrey, Harper and Pfeffer, 2012). Zdanowicz et al. (2012) reported a MAAT in the summit region of Penny Ice Cap of -16°C between 1992 and 2000. Based on a regression of the NCEP 700 hPa air temperatures against time, the MAAT rose by 0.8°C over the period 2000-2011. Firn temperatures at a depth of 10 m remained stable (-13°C) in measurements taken between 1953 and 2000. However, measurements taken at 9 m depth showed that the firn temperature rose by 10°C from 2000 to 2011. The observations at the Devon and Penny Ice Caps strongly suggest that

the recent rise in 10-15 m firn temperatures has been primarily driven by latent heat released by refreezing meltwater.

3.5 Summary and Conclusions

Airborne laser altimetry measurements made in 1995 and 2000 (Abdalati et al., 2004) showed that the higher elevation regions of the Devon Ice Cap were increasing in elevation. However, both airborne laser altimetry and field measurements show that the surface elevation in this region decreased between 2004 and 2012 and that net annual accumulation in the higher elevation regions of the Devon Ice Cap was increasingly being stored as either infiltration ice, or firn with a higher density than that which existed prior to 2004. Changes in firn stratigraphy, density, and temperature all indicate higher melt rates and increased infiltration and refreezing of meltwater within the firn layer. This strongly suggests that part of the surface height decreases detected by repeat altimetry measurements may be attributed to accelerated firn densification, rather than to mass loss.

Evidence of firn profile changes is found in the growth of thick ice layers in the uppermost 3 meters of the firn layer, and in the upward migration of the upper limit of >1 m thick multiyear ice layers from ~1300 m a.s.l. to ~1550 m a.s.l. An inflection is now evident in the 15 m firn depth-density profiles, with higher densities in the upper 3 m than in the region between 5 and 10 m depth. The average density of the top 2.5 m of firn has also increased sharply (by an average of 36% since 2004). As a result, firn depth-density profiles computed using Sorge's Law, no longer compare favorably with measured profiles. Calculated rates of change in the thickness of a 1.25 m w.e. layer of firn between 2004/2006 and 2012 ranged from -0.021 m a^{-1} to -0.168 m a^{-1}, and are significant in comparison to the magnitude of surface height changes derived from repeat airborne laser altimetry (-0.077 to -0.252 m a^{-1}). Air temperature changes and increased latent heat release by refreezing meltwater raised 10 m firn temperatures

near the ice cap summit from -23°C in 1971/1972 to -21.3°C in 2004 and -17.5°C in 2012. Of the observed 3.8°C rise in firn temperature since 2004, 1.0°C is attributable to increasing MAAT and 2.5°C is attributed to the increasing latent heat release from the refreezing of meltwater within the firn layer.

Earlier studies focusing on the response of Arctic glaciers and ice caps to climate warming suggested that they would be capable of self-buffering against a warming climate due to their thermal inertia and ability to absorb and retain meltwater within firn (Dowdeswell et al., 1997, Jansson, Hock, and Schneider, 2003). More recently, Harper et al. (2012) calculated the meltwater storage capacity of the Greenland Ice Sheet under the implicit assumption that the pore space of the entire firn column would ultimately be filled with infiltration ice. The firn layer of the Devon Ice Cap still provides a degree of buffering against rising air temperatures (because its pore volume has not yet been filled with infiltration ice and its temperature is still well below the freezing point). However, summer warming since 2005 has resulted in increased surface melting and major changes in the physical and thermal properties of the firn layer. These include the accumulation of decimeter to meter thick infiltration ice layers in the upper 4 m of firn (which continues to have spring temperatures well below freezing) and increases in 10-15 m firn temperatures that are driven primarily by the latent heat released by refreezing of the infiltrating meltwater.

Rising firn temperatures and densification of the upper layers of the firn will in time encourage more rapid densification below the depth to which meltwater percolates. Additionally, increased firn density and thicker ice layers will alter the thermal conductivity of the firn profile. The development of thick ice layers will also, and perhaps more significantly, change the path along which meltwater flows by increasing the resistance to vertical percolation and promoting the likelihood of supraglacial runoff and horizontal percolation. These changes have significant implications for interpreting

78

altimetrically-measured surface elevation changes in regions where, surface melt, infiltration and refreezing are occurring in terms of changes in climatic mass balance. Assuming that rates of snowfall and vertical strain remain unchanged, more rapid firn densification will cause thinning of the firn layer and lowering of the ice cap surface. Initial estimates for two locations on the Devon Ice Cap suggest that this process could account for between 77 and 90% of measured rates of surface lowering over the period of observation. Thus it is not safe to assume that lowering of the surface of high elevation regions of ice caps subject to climate warming necessarily (or simply) indicates loss of mass from those regions. Furthermore, the increase in ice content of the upper part of the firn since 2004 has reversed the vertical gradient of firn density as a function of depth. It now shows a trend of increasing density towards the surface. This reversal of the depth-density profile means that the use of Sorge's Law to estimate the density of firn inferred to have been removed from the ice cap during the period of surface warming is problematic.

Therefore, it is reasonable to conclude that outside the dry snow zone, in periods of climate warming (at least in their initial phases), estimation of rates of mass loss from measurements of surface elevation change in the accumulation zones of glaciers and ice caps is only possible if the temporal and spatial distribution of surface meltwater production, infiltration, and refreezing can be modeled reliably. While these processes are currently parameterized in existing models (e.g. Ettema and others, 2010), most of them assume homogeneous infiltration of meltwater into firn, while observations suggest that infiltration is commonly heterogeneous. In the absence of in situ measurements against which these models can be validated, studies have relied on inter-model comparison and sensitivity studies to test the quality of the parameterizations (Reijmer et al., 2012). This makes it very difficult to assess whether or not current models are adequate for the task, and suggests a need for both more field measurements of

changing firn properties during climate warming and a model inter-comparison exercise

designed to evaluate how well existing models can simulate observed changes.

	Melt Fraction (%)	
Site	2004/2005	2012
Colgan B (1625 m)	31.1	45.0
Colgan C (1825 m)	16.4	30.3
Colgan E (1525 m)	51.4	58.5

Table 3-1. Percent ice fraction calculated from w.e. for Colgan B, C, and E sites.

	Average density of a 2.5 m deep column of firn								
Site (elevation)	2000 (kg/m3)	2004 (kg/m3)	2005 (kg/m3)	2006 (kg/m3)	2008 (kg/m3)	2010 (kg/m3)	2011 (kg/m3)	2012 (kg/m3)	% change from first observation
Summit AWS (1900 m)	395					536		459	16.2
Site 1 (1800 m)		443					536	569	28.5
MB3-5 (1728 m)				485	437		513	548	13.0
MB5-8 (1686 m)				478	541		611	649	35.8
MB6-9 (1660 m)				455			554	641	40.8
MB8 (1635 m)				503			601	616	22.5
HB9-1 (1610 m)				514			625	620	20.6
MB10-3 (1575 m)				506	552		637	661	30.6
MB11-5 (1545 m)				575			676	711	23.7
MB12-6 (1510 m)				500	671		806	840	68.1
HB13-7 (1472 m)				551			729	821	49.0
MB14-8 (1460 m)				651			662	844	29.7
MB15-9 (1445 m)				544			861	828	52.4
Site 2 (1400 m)		705						855	21.3
Colgan B (1630 m)			450					812	80.3
Colgan C (1825 m)		361						572	58.2
Colgan E (1525 m)			598					731	22.2

Table 2-2. Average density of a 2.5 m deep column of firn.

82

Site (elevation)	Firn thickness (m) for 1.25 m w.e. deep layer			Thickness change (m)	Thickness change per annum (m a-1)
	2004-2006	2008	2012		
Site 1 (1800 m)	2.73		2.56	-0.17	-0.021
MB3-5 (1728 m)	2.56	2.84	2.29	-0.27	-0.045
MB5-8 (1686 m)	2.6	2.25	1.87	-0.73	-0.122
MB6-9 (1660 m)	2.71		1.99	-0.72	-0.120
MB8 (1635 m)	2.49		1.98	-0.51	-0.085
HB9-1 (1610 m)	2.44		1.98	-0.46	-0.077
MB10-3 (1575 m)	2.47	2.28	1.76	-0.71	-0.118
MB11-5 (1545 m)	2.44		1.7	-0.74	-0.123
MB12-6 (1510 m)	2.5	1.99	1.49	-1.01	-0.168
HB13-7 (1472 m)	2.3		1.6	-0.7	-0.117
MB14-8 (1460 m)	2.14		1.48	-0.66	-0.110
MB15-9 (1440 m)	2.38		1.51	-0.87	-0.145
Site 2 (1400 m)	1.95		1.46	-0.49	-0.061
Colgan B (1630 m)	2.74		1.59	-1.15	-0.164
Colgan C (1825 m)	3.28		2.35	-0.93	-0.116
Colgan E (1525 m)	1.93		1.66	-0.27	-0.039

Table 3-3. Firn thickness calculated from the density profile of a 1 m2 surface layer that is 1.25 m w.e. deep.

Elevation (m)	Calculated firn thickness change (m a-1)	Measured surface height change (m a-1)	% of thickness change in height change
1750-1850	-0.069	-0.077	89
1650-1750	-0.096	-0.125	77
1550-1650	-0.087	-0.193	45
1450-1550	-0.130	-0.240	54
1350-1450	-0.103	-0.252	41

Table 3-4. Comparison of calculated firn thickness changes from Table 3 and surface

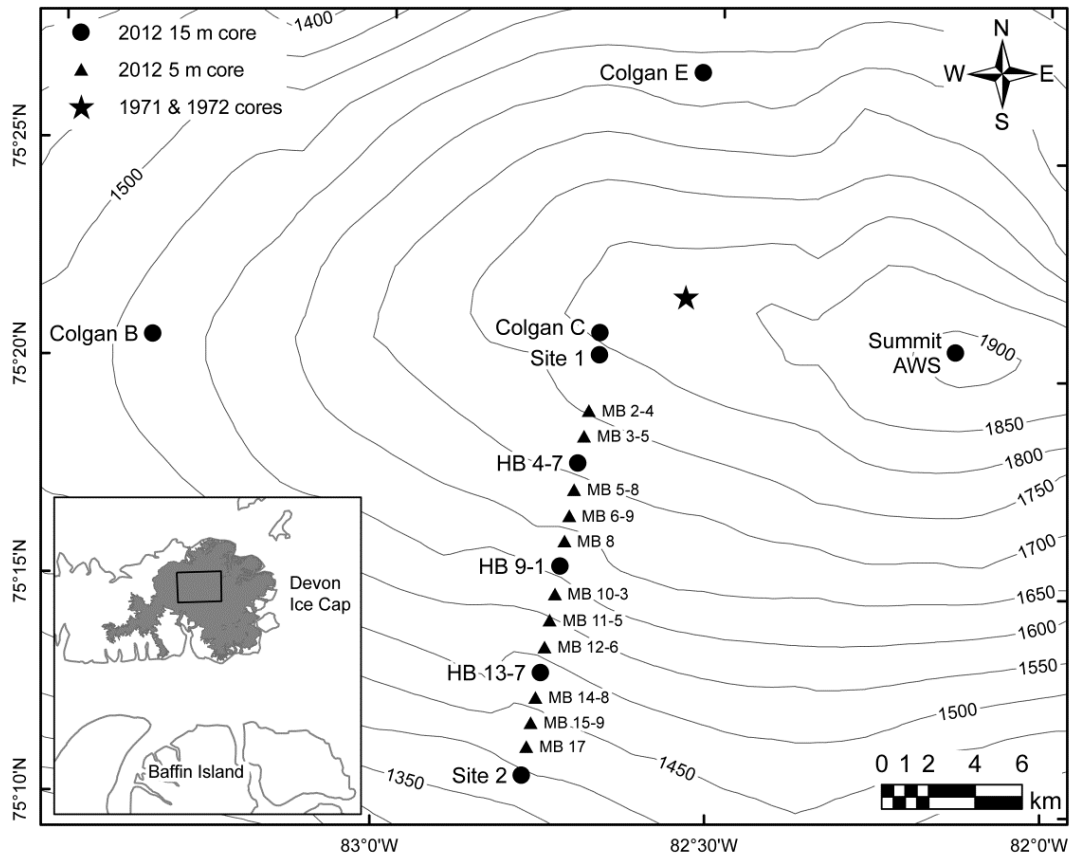height changes measured by repeat airborne laser altimetry for the period 2004-2012.

Figure 3-1. Devon Ice Cap location and fieldwork sites. Between Site 1 and Site 2, MB indicated a mass balance stake, and HB indicates a mass balance stake with a HOBO air temperature sensor. The proceeding numbers indicates the approximate kilometers from Site 1. At least two cores were recovered at every site indicated with a circle or a triangle.
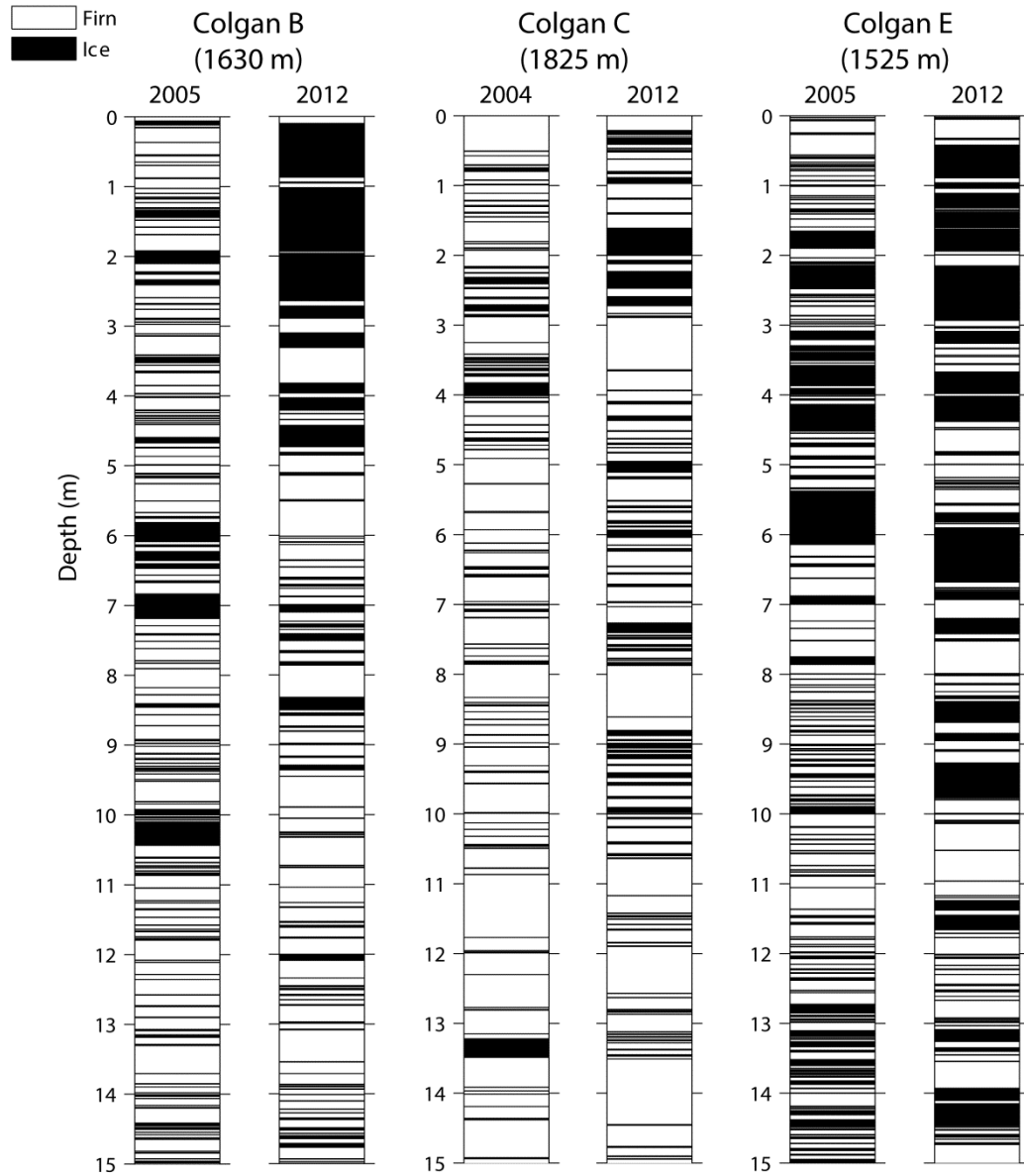
Figure 3-2. Comparison of 15 m 2004/2005 vs. 2012 firn stratigraphy at Colgan B, C, and E sites.

Figure 3-3. Comparison of 3 m 2004/2006 vs. 2012 firn stratigraphy at selected sites along the CryoSat Line. Grey indicates no data, where the 2006 cores were less then three meters.
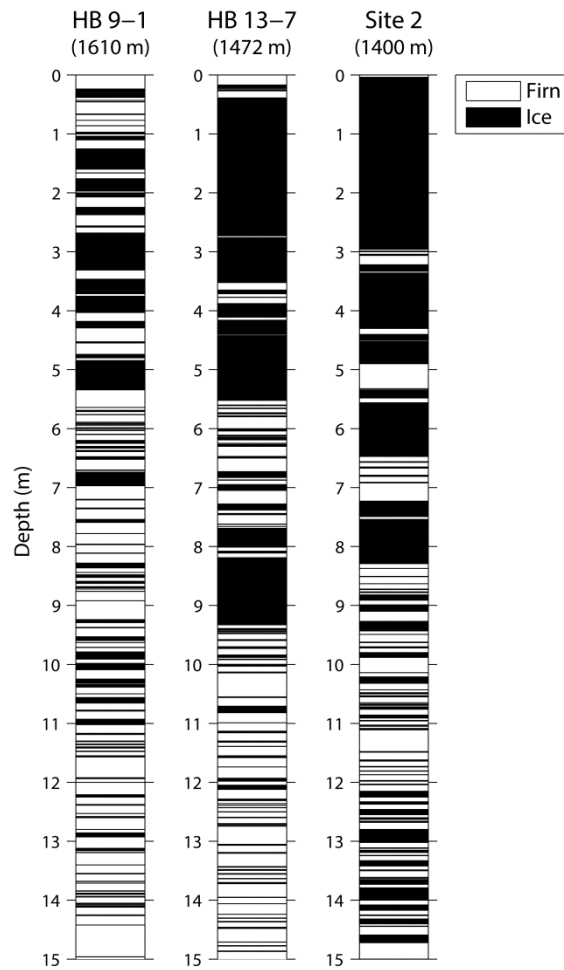
Figure 3-4. 2012 15 m firn stratigraphy at HB 9-1, HB 13-7 and Site 2 on the CryoSat line. Fifteen meters of firn stratigraphy represent at least 50 years of net accumulation allowing for a comparison of decadal scale changes in summer melt conditions.

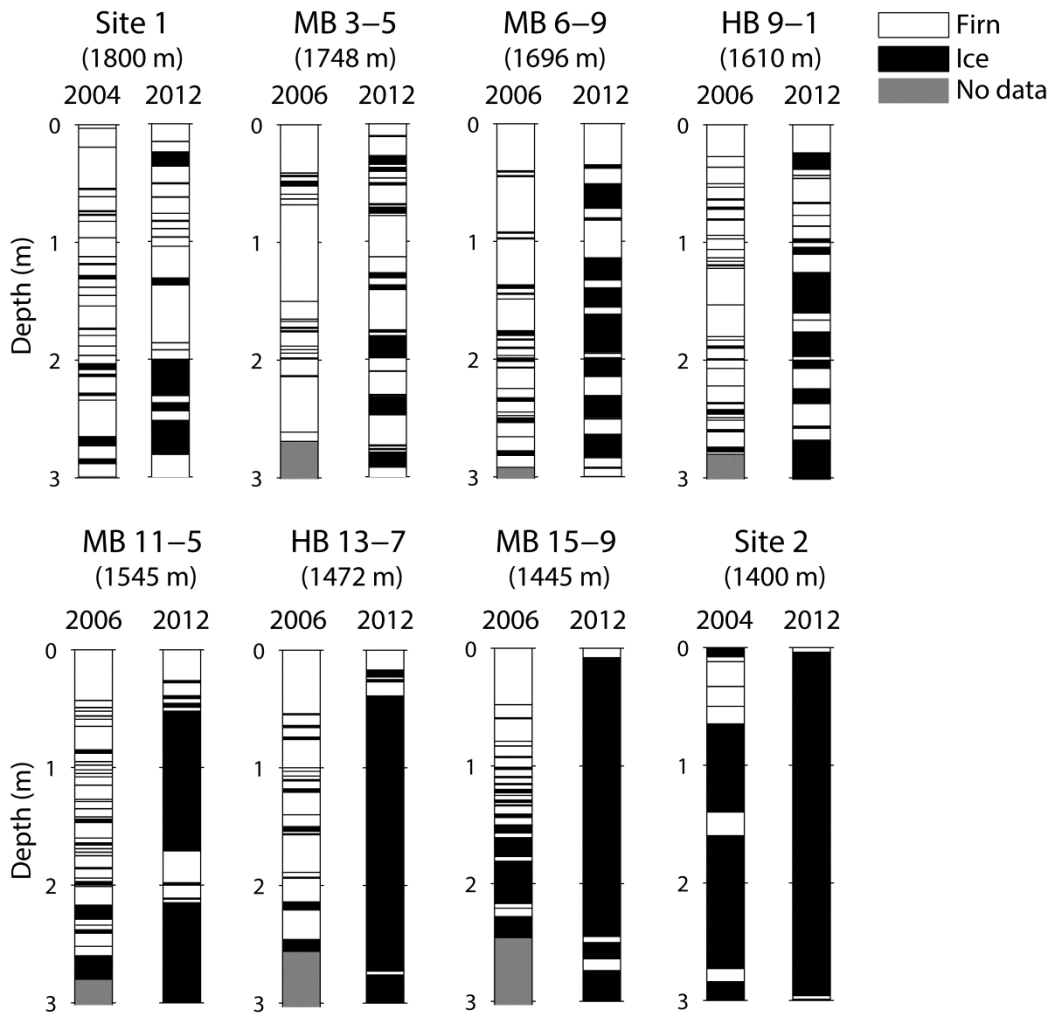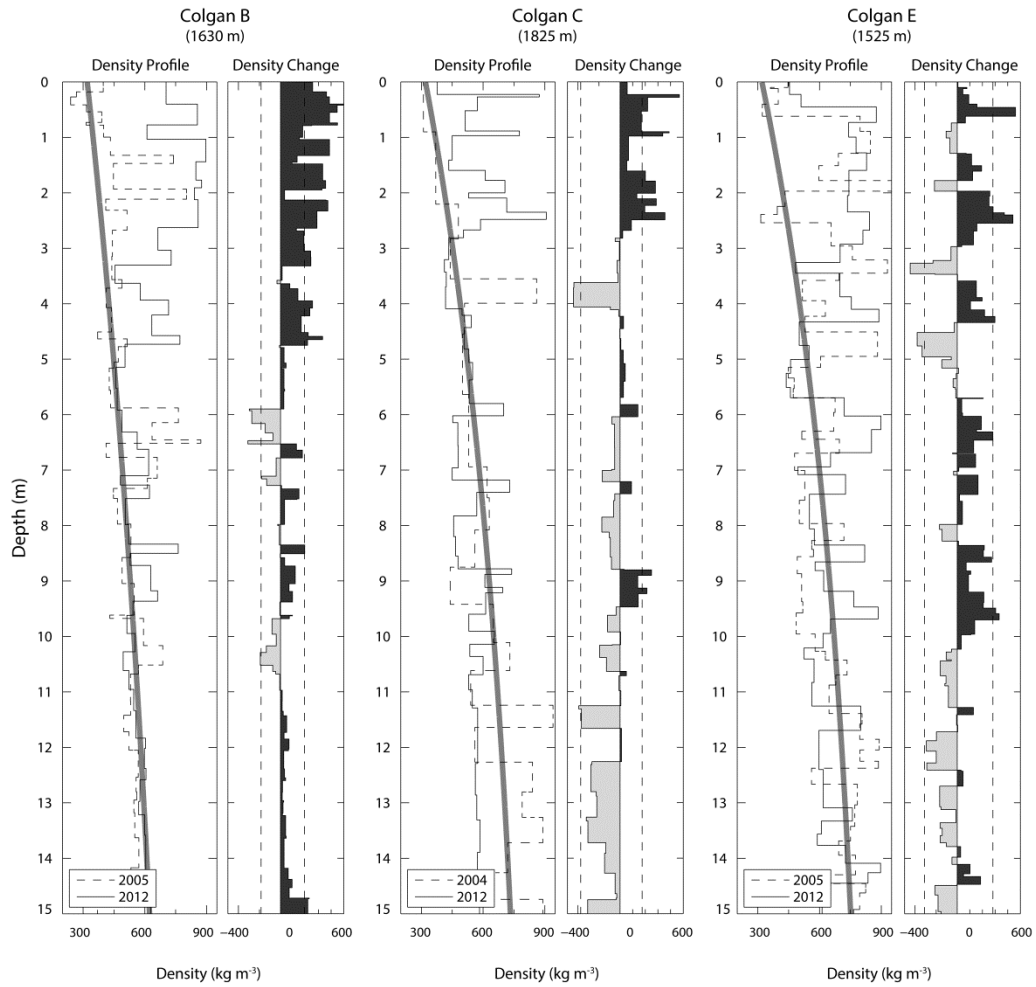Figure 3-5. Measured and empirically derived (thick grey line) firn density profiles for Colgan B, C, and E sites. The firn density change is the 2012 firn density less the 2004/2005 firn density. The dashed lines represent ±2 standard deviations from the mean change of the bottom 10 m.
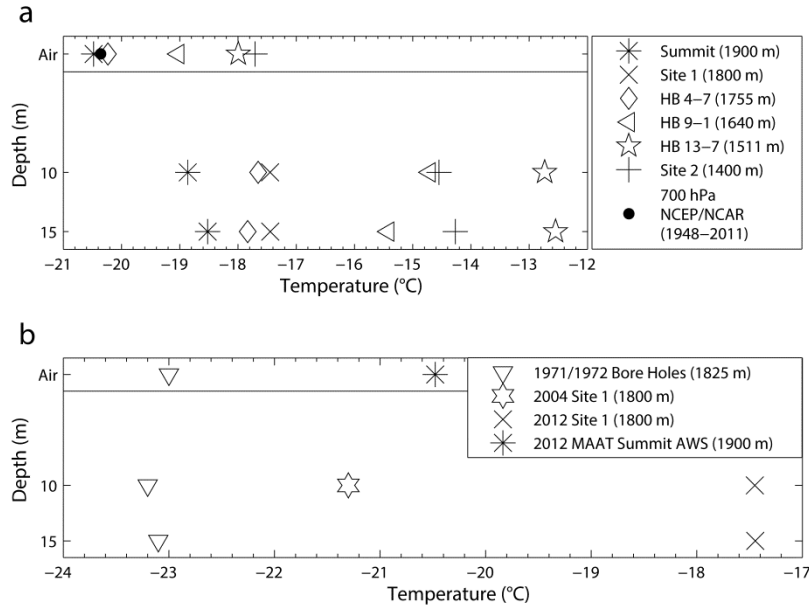
Figure 3-6. A) MAAT and firn temperatures across the elevation range of the accumulation zone. B) MAAT and firn temperature observations on the summit plateau for 1971/1972, 2004 and 2012.

Figure 3-7. NCEP 700 mbar MAAT for the summit region of Devon Ice Cap

3.6 References

Abdalati, W., Krabill, W., Frederick, E., Manizade, S., Martin, C., Sonntag, J., et al. (2004). Elevation changes of ice caps in the Canadian Arctic Archipelago. *Journal of Geophysical Research: Earth Surface (2003–2012), 109*(F4).

Bader, H. (1954). Sorge's law of densification of snow on high polar glaciers. *J.Glaciol, 2*(15), 319-323.

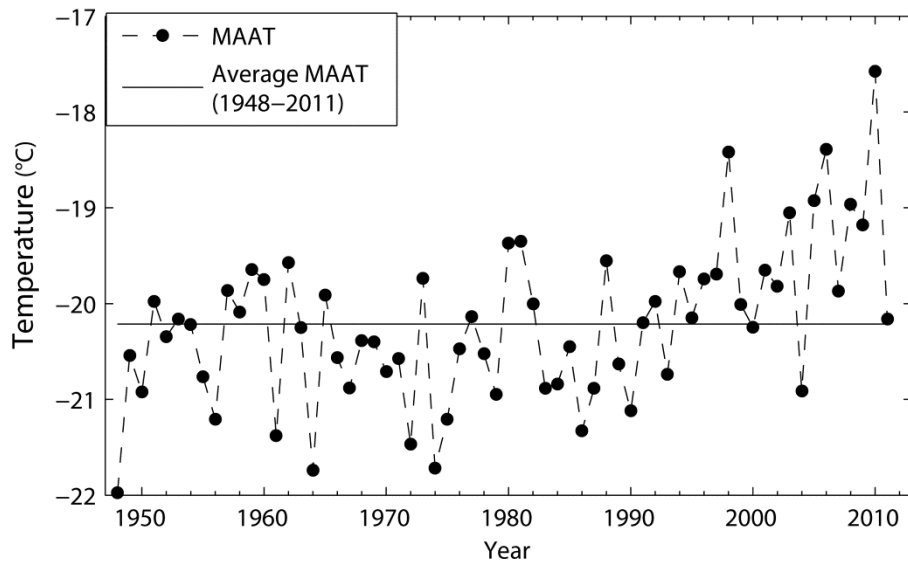Bell, C., Mair, D., Burgess, D., Sharp, M., Demuth, M., Cawkwell, F., et al. (2008). Spatial and temporal variability in the snowpack of a high Arctic ice cap: Implications for mass-change measurements. *Annals of Glaciology, 48*(1), 159-170.

Boon, S., Burgess, D. O., Koerner, R. M., & Sharp, M. J. (2010). Forty-seven years of research on the Devon Island Ice Cap, Arctic Canada. *Arctic,*13-29.

Burgess, D. O., Sharp, M. J., Mair, D. W., Dowdeswell, J. A., & Benham, T. J. (2005). Flow dynamics and iceberg calving rates of Devon Ice Cap, Nunavut, Canada. *Journal of Glaciology, 51*(173), 219-230.

Colgan, W., Davis, J., & Sharp, M. (2008). Is the high-elevation region of Devon Ice Cap thickening? *Journal of Glaciology, 54*(186), 428-436.

Colgan, W., & Sharp, M. (2008). Combined oceanic and atmospheric influences on net accumulation on Devon Ice Cap, Nunavut, Canada. *Journal of Glaciology, 54*(184), 28-40.

Cuffey, K. M., & Paterson, W. S. B. (2010). *The physics of glaciers* Access Online via Elsevier.

Dowdeswell, J. A., Hagen, J. O., Björnsson, H., Glazovsky, A. F., Harrison, W. D., Holmlund, P., et al. (1997). The mass balance of circum-Arctic glaciers and recent climate change. *Quaternary Research, 48*(1), 1-14.

Ettema, J., Broeke, M., Meijgaard, E. v., Berg, W., Box, J., & Steffen, K. (2010). Climate of the Greenland Ice Sheet using a high-resolution climate model–Part 1: Evaluation. *The Cryosphere, 4*(4), 511-527.

Fisher, D., Zheng, J., Burgess, D., Zdanowicz, C., Kinnard, C., Sharp, M., et al. (2012). Recent melt rates of Canadian Arctic Ice Caps are the highest in four millennia. *Global and Planetary Change, 84*, 3-7.

Gardner, A. S., Moholdt, G., Wouters, B., Wolken, G. J., Burgess, D. O., Sharp, M. J., et al. (2011). Sharply increased mass loss from glaciers and ice caps in the Canadian Arctic Archipelago. *Nature, 473*(7347), 357-360.

Gardner, A. S., & Sharp, M. (2007). Influence of the arctic circumpolar vortex on the mass balance of Canadian high Arctic glaciers. *Journal of Climate, 20*(18), 4586-4598.

Harper, J., Humphrey, N., Pfeffer, W., Brown, J., & Fettweis, X. (2012). Greenland Ice Sheet contribution to sea-level rise buffered by meltwater storage in firn. *Nature, 491*(7423), 240-243.

Hörhold, M., Kipfstuhl, S., Wilhelms, F., Freitag, J., & Frenzel, A. (2011). The densification of layered polar firn. *Journal of Geophysical Research: Earth Surface (2003–2012), 116*(F1)

Humphrey, N. F., Harper, J. T., & Pfeffer, W. T. (2012). Thermal tracking of meltwater retention in Greenland's accumulation area. *Journal of Geophysical Research: Earth Surface (2003–2012), 117*(F1)

Jansson, P., Hock, R., & Schneider, T. (2003). The concept of glacier storage: A review. *Journal of Hydrology, 282*(1), 116-129.

Kalnay, E., Kanamitsu, M., Kistler, R., Collins, W., Deaven, D., Gandin, L., et al. (1996). The NCEP/NCAR 40-year reanalysis project. *Bulletin of the American Meteorological Society, 77*(3), 437-471.

Koerner, R. (1970). Some observations on superimposition of ice on the Devon Island Ice Cap, NWT Canada. *Geografiska Annaler.Series A.Physical Geography, ,* 57-67.

Koerner, R. M. (2005). Mass balance of glaciers in the Queen Elizabeth Islands, Nunavut, Canada. *Annals of Glaciology, 42*(1), 417-423.

Koerner, R. M. (1977). Devon Island Ice Cap: Core stratigraphy and paleoclimate. *Science, 196*(4285), 15-18.

Mair, D., Burgess, D., & Sharp, M. (2005). Thirty‐seven year mass balance of Devon Ice Cap, Nunavut, Canada, determined by shallow ice coring and melt modeling. *Journal of Geophysical Research: Earth Surface (2003–2012), 110*(F1).

Oerlemans, J., & Reichert, B. (2000). Relating glacier mass balance to meteorological data by using a seasonal sensitivity characteristic. *Journal of Glaciology, 46*(152), 1-6.

Paterson, W., & Clarke, G. (1978). Comparison of theoretical and observed temperature profiles in Devon Island Ice Cap, Canada. *Geophysical Journal of the Royal Astronomical Society, 55*(3), 615-632.

Paterson, W., Koerner, R., Fisher, D., Johnsen, S., Clausen, H., Dansgaard, W., et al. (1977). An oxygen-isotope climatic record from the Devon Island Ice Cap, Arctic Canada. *Nature, 266,* 508-511.

Pfeffer, W., & Humphrey, N. (1998). Formation of ice layers by infiltration and refreezing of meltwater. *Annals of Glaciology, 26,* 83-91.

Pohjola, V. A., Martma, T. A., Meijer, H. A., Moore, J. C., Isaksson, E., Vaikmae, R., et al. (2002). Reconstruction of three centuries of annual accumulation rates based on the record of stable isotopes of water from Lomonosovfonna, Svalbard. *Annals of Glaciology, 35*(1), 57-62.

Reijmer, C., van den Broeke, M., Fettweis, X., Ettema, J., & Stap, L. (2012). Refreezing on the Greenland Ice Sheet: A comparison of parameterizations. *Cryosphere (the), 6.*

Sharp, M., Burgess, D. O., Cogley, J. G., Ecclestone, M., Labine, C., & Wolken, G. J. (2011). Extreme melt on Canada's Arctic Ice Caps in the 21st century. *Geophysical Research Letters, 38*(11).

Zdanowicz, C., Smetny‐Sowa, A., Fisher, D., Schaffer, N., Copland, L., Eley, J., et al. (2012). Summer melt rates on Penny Ice Cap, Baffin Island: Past and recent trends and implications for regional climate. *Journal of Geophysical Research: Earth Surface (2003–2012), 117*(F2)

Chapter 4

4.1 Summary

Since the mid-2000s, a rapid ablation of the Arctic cryosphere has been observed, as evidenced by decreased fall sea ice extent, decreased spring snow cover extent and reductions in glacier mass (Gardner et al., 2011; Hanna et al., 2011; Sharp et al., 2011; Derksen and Brown, 2012; Wang and Overland, 2012). For the Canadian Arctic Archipelago (CAA), recent glacier mass losses are particularly important because the region has emerged as the largest non-ice sheet source of eustatic sea level rise (Gardner et al., 2011, 2013; Lenaerts et al., 2013). Coincident with the rapid ablation of the cryosphere since the mid-2000s, has been a transition in summer atmospheric circulation patterns towards more frequent and persistent anticyclonic circulation over Greenland and the CAA (Overland et al., 2012; Fettweis et al., 2013; Hanna et al., 2013). Summer atmospheric circulation is a major driver of glacier mass balance variability in the CAA as the interannual variability of winter accumulation is low, while the interannual variability of summer air temperatures is high (Oerlemans & Reichert, 2000; Braithwaite, 2005; Koerner, 2005).

Chapter 2 expands on Alt (1978, 1979 & 1987) and Gascon et al., (2013) and evaluates the past and potential future variability of summer anticyclonic atmospheric circulation over the CAA and western Greenland as recorded in the National Centers for Environmental Prediction and the National Center for Atmospheric Research Reanalysis 1 (NCEP) (1948-2012) and simulated by five Coupled Model Intercomparison Project Phase 5 (CMIP5) climate models (1950-2025) forced by historic and future emissions scenarios. Future emissions scenarios are described by the Representative Concentration Pathways (RCP) 8.5 (Meinshausen et al., 2011). RCP8.5 prescribes greenhouse gas concentrations, air pollutants and land use changes that increase the global radiative forcing from ~2.2 W m^{-2} in 2005 to 8.5 W m^{-2} by 2100. The Self Organizing Map (SOM) approach was used to classify historic and future patterns and

trends in daily summer 500 hPa GPH anomaly fields. NCEP results show relatively low amplitudes of inter-annual and multi-decadal variability of summer anticyclonic circulation over western Greenland and the CAA between 1948 and 2007. Between 2007 and 2012,however, the mean frequency and duration of anticyclonic circulation episodes doubled, and exceeded two standard deviations above the climatological means (1951-2010). While this dramatic change in summer atmospheric circulation frequency and duration since 2007 is evident in NCEP reanalysis, the five CMIP5 models evaluated did not at any point in the 1950-2025 time period generate an anticyclonic circulation frequency anomaly similar to that seen in the NCEP data.

To diagnose potential drivers and predictors of variability in NCEP summer anticyclonic circulation patterns over western Greenland and the CAA between 1979 and 2012, a series of correlation and multiple linear regression analyses were conducted between the frequency of positive summer 500 hPa geopotential height (GPH) anomalies over Greenland and the CAA, pan-Arctic sea ice extent and volume, northern hemisphere snow cover (SCE) extent, and meridional heat advection. Between 1979 and 2012, April, May and June decreasing sea ice volume was the most significant predictor of more frequent positive summer 500 hPa GPH anomalies over western Greenland and the CAA. June meridional heat advection was also a statistically significant predictor of positive summer 500 hPa GPH anomalies. Sea ice extent and northern hemisphere SCE in June, July and August were highly correlated (-0.44 to -0.74, $p<0.01$) with summer 500 hPa GPH anomalies, but they were not found to be significant predictors of summer 500 hPa GPH anomalies in the multiple linear regression models.

Given the increase in the frequency and persistence of summer anticyclonic circulation over the CAA since the mid-2000s, it was hypothesized that more intense summer melt conditions (Sharp et al., 2011; Gascon et al., 2013) would have resulted in observable changes in the distribution of surface snow facies, and in the density and temperature

profiles of firn in the accumulation zone of the Devon Ice Cap, Nunavut. In 2012, 20 firn cores were recovered from sites previously cored between 2004 and 2011. Firn stratigraphy, ice fraction and density profiles revealed significant increases in the ice content and bulk density of the top three meters of the firn profile which are attributable to increased surface meltwater percolation and refreezing within the upper layers of the firn. Firn temperatures at 1800 m a.s.l. rose 3.8°C between 2004 and 2012. Of this 3.8°C increase in firn temperature, 2.8°C is attributable to the latent heat released by the increase in meltwater refreezing and 1°C is attributable to the observed change in the mean annual air temperature.

As glacier surface height changes measured by repeat airborne/satellite laser altimetry are commonly used to calculate glacier mass changes, it is important to assess how changes in the rate of firn densification may have contributed to measured changes in ice cap surface height. Height changes caused by this effect would not have resulted in any change in ice cap mass. Observed firn density profiles were therefore compared with firn density profiles derived empirically on the assumption that annual accumulation and melt rates are constant over time. This comparison showed that the empirically derived profiles no longer match the firn density profiles measured on the Devon Ice Cap. For the region above 1750 m a.s.l., a comparison of the surface height changes measured by airborne laser altimetry between 2004 and 2012 with those that would have resulted from more rapid firn densification alone indicated that the measured height changes can be explained almost entirely by increases in the densification rate of the top ~3 m of the firn profile.

4.2 Contributions and future research

The atmospheric circulation and firn profile changes reported here raise several important questions that could be explored in future work. In light of the nonlinear trends evident in other metrics of high latitude atmospheric circulation, such as the North

Atlantic Oscillation (NAO) Index, a higher order method is required to classify the daily atmospheric circulation patterns observed between 1948 and 2012. The SOM based classification of daily 500 hPa GPH anomaly fields over the CAA and western Greenland provides a more robust atmospheric circulation classification method than the statistical classification methods used by Belleflamme et al. (2012), Hanna et al. (2012), Overland et al. (2012), and Fettweis et al. (2013). Belleflame et al. (2012) and Fettweis et al. (2013) applied a correlation based circulation type classification (CTC) method where the daily 500 hPa GPH anomaly fields are grouped according to the strength of their correlations. Patterns that are highly correlated are grouped together into the first class, while the remaining daily GPH fields are then correlated to generate the next generalized pattern. In these analyses, the number of classes generated ranges from three (Fettweis et al., 2013) to eight (Belleflame et al., 2012). Using the CTC method with such a low number of classes is likely to hide non-linear shifts in atmospheric circulation patterns, as rare or extreme atmospheric circulation patterns are averaged into very large classes. Evidence for this can be found in the empirical orthogonal function (EOF) analysis of the daily summer NCEP 500 hPa GPH anomalies over the CAA and western Greenland, which was presented in Chapter 2. The first three and eight EOFs account for 35% and 50% of the cumulative explained variance, respectively, leaving a very large portion of unexplained variance. Overland et al. (2012) and Hanna et al. (2012) used no classification method, choosing rather to create composite means of GPH fields for specific periods of interest, ranging from monthly/summer means (one year) to multiple monthly/summer means (6-7 years). In the above examples, it is possible that the low number of generalized circulation patterns may incorporate and hide subtle, nonlinear shifts in the frequency of anticyclonic circulation. If the rare and extreme events become hidden within a classification group with a high degree of internal variability, extracting the frequency of rare and extreme events becomes extremely challenging when evaluating multiple years of high temporal resolution (daily or greater) climate data.

While the SOM has advantages in terms of its ability to capture rare and extreme events, it is limited by the amount of computer memory that is required to compute the SOM algorithm. For example, SOM analysis of the daily summer Northern Hemisphere GPH fields from NCEP and the five climate models analyzed here required a numerical server with a minimum of 75 gigabytes (GB) of memory. Studies requiring a larger cohort of climate models (Belleflame et al. (2012) used 35 models), may find it challenging to access the amount of computer memory required to compute the SOM. Therefore, less computationally demanding classification methods are still needed if the model cohort is large. Here, in the study of previously unobserved circulation regimes, the SOM is expected to produce a more robust classification method than the previously discussed EOF and CTC methods (Reusch et al., 2005; Reusch, 2010).

To date, no analysis has investigated the combined influence of declining Arctic sea ice extent and volume, decreased northern hemisphere SCE, and meridional heat advection on the frequency of anticyclonic circulation over the CAA and western Greenland in summer. However, these parameters have all been hypothesized as drivers of anticyclonic circulation variability (Serreze & Barry, 2011; Francis & Vavrus, 2012; Overland et al., 2012; Screen et al. 2012). Therefore, the first step toward identifying a physical mechanism behind the changes in the frequency of the anomalous anticyclonic circulation observed over the CAA and western Greenland between 2007 and 2012, is to use the SOM results to evaluate the relative influences of Arctic sea ice extent and volume, northern hemisphere SCE, and meridional heat advection on anticyclonic circulation variability between 1979 and 2012. Keeping in mind that the correlation and multiple linear regression analyses presented in Chapter 2 yield statistical, rather than physical, relationships, it is important to investigate whether these relationships are consistent with the results of simulations performed using physical models. A first step in that direction could be to conduct an analysis using atmospheric

circulation models forced with surface observations, which is similar to the methodology discussed in Chapter 2. Currently, CMIP5 includes such model runs, but only for the period 1979-2009. Dedicated runs with an atmospheric circulation model forced with surface observations are another option. One benefit of this approach would be the ability to undertake a sensitivity analysis by systematically perturbing Arctic sea ice extent and thickness, and northern hemisphere SCE in order to determine their individual and combined influences on Arctic atmospheric circulation.

The work presented in Chapter 3 contributes to investigations of ice cap mass balance that are based on repeat altimetric measurements of glacier surface height. In such investigations, the firn layer is generally described as being either a uniform layer with a single density (Gardner et al., 2011) or a non-uniform layer with a depth-density profile that reflects steady-state climatic conditions (Moholdt et al., 2010). Neither approach is defensible under conditions of systematically changing atmospheric temperatures. The work presented in Chapter 3 shows that firn profiles on the Devon Ice Cap underwent a significant change between 2004 and 2012, and that widely used empirically-derived firn density profiles are unable to accurately represent that change. While our understanding of the firn profile response to anomalously high melt rates on the Devon Ice Cap since 2005 is good, this work needs to be expanded to include more ice caps and glaciers in the CAA as well as the Greenland Ice Sheet.

On the Devon Ice Cap, the formation of ice layers with water equivalent thicknesses amounting to more than one year of net annual accumulation is primarily responsible for the density increases in the upper 3 m of the firn profile. The development of multiyear ice layers near the surface suggests that vertical percolation of meltwater is likely being retarded and that the growing ice layers may isolate the underlying firn from surface-derived meltwater. One challenge in assessing the results presented in Chapter 3 is the discrete manner in which coring samples the firn profile. Fortunately, ground penetrating

radar (GPR) surveys made between 2007 and 2012 confirm that the ice layers are continuous across most of the accumulation zone (Gascon et al., in review). The assumption that the Devon Ice Cap firn layer is now impermeable to vertical percolation over much of the accumulation zone raises a serious question about where the meltwater produced in the accumulation zone is located at the end of the melt season. Potentially, meltwater from the accumulation zone could either flow off the ice cap, pool and refreeze on the surface of the ice cap, or find a path through the multiyear ice layers, reaching previously unfilled pore space in the underlying firn. All three of these scenarios have distinct implications for the computation of glacier mass balance on annual and decadal scales.

4.3 References

Alt, B. T. (1978). Synoptic climate controls of mass-balance variations on Devon Island Ice Cap. *Arctic and Alpine Research,* 61-80.

Alt, B. T. (1979). Investigation of summer synoptic climate controls on the mass balance of Meighen Ice Cap. *Atmosphere-Ocean, 17*(3), 181-199.

Alt, B. T. (1987). Developing synoptic analogs for extreme mass balance conditions on Queen Elizabeth Island Ice Caps. *Journal of Applied Meteorology, 26*, 1605-1623.

Belleflamme, A., Fettweis, X., Lang, C., & Erpicum, M. (2012). Current and future atmospheric circulation at 500 hPa over Greenland simulated by the CMIP3 and CMIP5 global models. *Climate Dynamics,* 1-20.

Braithwaite, R. J. (2005). Mass-balance characteristics of Arctic glaciers. *Annals of Glaciology, 42*(1), 225-229.

Derksen, C., & Brown, R. (2012). Spring snow cover extent reductions in the 2008–2012 period exceeding climate model projections. *Geophysical Research Letters, 39*(19).

Fettweis, X., Hanna, E., Lang, C., Belleflamme, A., Erpicum, M., & Gallée, H. (2013). Important role of the mid-tropospheric atmospheric circulation in the recent surface melt increase over the Greenland Ice Sheet. *Cryosphere (the), 7.*

Francis, J. A., & Vavrus, S. J. (2012). Evidence linking arctic amplification to extreme weather in mid‐latitudes. *Geophysical Research Letters, 39*(6).

Gardner, A. S., Moholdt, G., Cogley, J. G., Wouters, B., Arendt, A. A., Wahr, J., et al. (2013). A reconciled estimate of glacier contributions to sea level rise: 2003 to 2009. *Science, 340*(6134), 852-857.

Gardner, A. S., Moholdt, G., Wouters, B., Wolken, G. J., Burgess, D. O., Sharp, M. J., et al. (2011). Sharply increased mass loss from glaciers and ice caps in the Canadian Arctic Archipelago. *Nature, 473*(7347), 357-360.

Gascon, G., Sharp, M., & Bush, A. (2013). Changes in melt season characteristics on Devon Ice Cap, Canada, and their association with the arctic atmospheric circulation. *Annals of Glaciology, 54*, 101-110.

Hanna, E., Fettweis, X., Mernild, S. H., Cappelen, J., Ribergaard, M. H., Shuman, C. A., et al. (2013). Atmospheric and oceanic climate forcing of the exceptional Greenland Ice Sheet surface melt in summer 2012. *International Journal of Climatology.*

Hanna, E., Jones, J. M., Cappelen, J., Mernild, S. H., Wood, L., Steffen, K., et al. (2012). The influence of North Atlantic atmospheric and oceanic forcing effects on 1900–2010 Greenland summer climate and ice melt/runoff. *International Journal of Climatology.*

Koerner, R. M. (2005). Mass balance of glaciers in the Queen Elizabeth Islands, Nunavut, Canada. *Annals of Glaciology, 42*(1), 417-423.

Lenaerts, J., Angelen, J. H., Broeke, M. R., Gardner, A. S., Wouters, B., & Meijgaard, E. (2013). Irreversible mass loss of Canadian Arctic Archipelago glaciers. *Geophysical Research Letters 40.*

Meinshausen, M., Smith, S. J., Calvin, K., Daniel, J. S., Kainuma, M., Lamarque, J., et al. (2011). The RCP greenhouse gas concentrations and their extensions from 1765 to 2300. *Climatic Change, 109*(1-2), 213-241

Moholdt, G., Nuth, C., Hagen, J. O., & Kohler, J. (2010). Recent elevation changes of Svalbard glaciers derived from ICESat laser altimetry. *Remote Sensing of Environment, 114*(11), 2756-2767.

Oerlemans, J., & Reichert, B. (2000). Relating glacier mass balance to meteorological data by using a seasonal sensitivity characteristic. *Journal of Glaciology, 46*(152), 1-6.

Overland, J. E., Francis, J. A., Hanna, E., & Wang, M. (2012). The recent shift in early summer Arctic atmospheric circulation. *Geophysical Research Letters, 39*(19).

Reusch, D. B. (2010). Nonlinear climatology and paleoclimatology: Capturing patterns of variability and change with self-organizing maps. *Physics and Chemistry of the Earth, Parts A/B/C, 35*(9), 329-340.

Reusch, D. B., Alley, R. B., & Hewitson, B. C. (2005). Relative performance of self-organizing maps and principal component analysis in pattern extraction from synthetic climatological data. *Polar Geography, 29*(3), 188-212.

Screen, J. A., Simmonds, I., Deser, C., & Tomas, R. (2012). The atmospheric response to three decades of observed Arctic sea ice loss. *Journal of Climate,* (2012)

Serreze, M. C., & Barry, R. G. (2011). Processes and impacts of arctic amplification: A research synthesis. *Global and Planetary Change, 77*(1), 85-96.

Sharp, M., Burgess, D. O., Cogley, J. G., Ecclestone, M., Labine, C., & Wolken, G. J. (2011). Extreme melt on Canada's Arctic ice caps in the 21st century. *Geophysical Research Letters, 38*(11)

Wang, M., & Overland, J. E. (2012). A sea ice free summer Arctic within 30 years: An update from CMIP5 models. *Geophysical Research Letters, 39*(18)